

2



Naval Research Laboratory

Washington, DC 20375-5000

NRL Memorandum Report 6172

DTIC FILE COPY

AD-A199 734

**Halo Formation and Hollowing in
Relativistic Electron Beams**

**RICHARD F. HUBBARD, MARTIN LAMPE,
STEVEN P. SLINKER, AND GLENN JOYCE**

*Plasma Theory Branch
Plasma Physics Division*

**DTIC
ELECTE
SEP 23 1988
D⁰² D**

August 10, 1988

SECURITY CLASSIFICATION OF THIS PAGE

REPORT DOCUMENTATION PAGE				Form Approved OMB No 0704-0188	
1a REPORT SECURITY CLASSIFICATION UNCLASSIFIED			1b RESTRICTIVE MARKINGS		
2a SECURITY CLASSIFICATION AUTHORITY			3 DISTRIBUTION / AVAILABILITY OF REPORT		
2b DECLASSIFICATION / DOWNGRADING SCHEDULE			Approved for public release; distribution unlimited.		
4 PERFORMING ORGANIZATION REPORT NUMBER(S) NRL Memorandum Report 6172			5 MONITORING ORGANIZATION REPORT NUMBER(S)		
6a NAME OF PERFORMING ORGANIZATION Naval Research Laboratory		6b OFFICE SYMBOL (If applicable) Code 4790	7a NAME OF MONITORING ORGANIZATION Naval Surface Warfare Center		
6c ADDRESS (City, State, and ZIP Code) Washington, DC 20375-5000			7b ADDRESS (City, State, and ZIP Code) Silver Spring, MD 20903-5000		
8a NAME OF FUNDING SPONSORING ORGANIZATION DARPA		8b OFFICE SYMBOL (If applicable)	9 PROCUREMENT INSTRUMENT IDENTIFICATION NUMBER JO# 47-0900-0-7		
8c ADDRESS (City, State, and ZIP Code) Arlington, VA 22209			10 SOURCE OF FUNDING NUMBERS	PROGRAM ELEMENT NO	PROJECT ARPA NO ORDER
			62707E	#4395-A69	TASK NO
			WORK UNIT ACCESSION NO	DN180-127	
11 TITLE (Include Security Classification) Halo Formation and Hollowing in Relativistic Electron Beams					
12 PERSONAL AUTHOR(S) Hubbard, Richard F., Lampe, Martin, Slinker, Steven P., and Joyce, Glenn					
13a TYPE OF REPORT Interim		13b TIME COVERED FROM _____ TO _____	14 DATE OF REPORT (Year, Month, Day) 1988 August 10		15 PAGE COLUMN 63
16 SUPPLEMENTARY NOTATION <i>and ...</i>					
17 COSAC CODES			18 SUBJECT TERMS (Continue on reverse if necessary and identify by block number)		
FIELD	GROUP	SUB-GROUP	Relativistic electron beam, Return current, Resistive instability, Hollowing, Hose instability,		
19 ABSTRACT (Continue on reverse if necessary and identify by block number) A relativistic electron beam propagating through dense gas may evolve to a variety of current density profiles $J_b(r)$ depending on the beam temperature T and plasma current profile $J_p(r)$. We have identified four broad classes of equilibria in particle simulations: (1) Bennett-like or compact, (2) core and halo, (3) on-axis hollowed and (4) off-axis hollowed. The qualitative features of each class are reproduced in a simple analytical model which assumes an isothermal beam and a Bennett plasma current profile and iterates about an initial ansatz of a Bennett beam current profile. Bennett-like equilibria are produced when the return current fraction f is small or when $T/T_B = 1-f$, where $T_B = eI_b/2c$ is the Bennett temperature. For $T/T_B > 1-f$ and moderate or high f , the equilibrium consists of a compact core surrounded by a halo which may contain most of the beam current. In extreme cases ($T/T_B \gg 1-f$ and f close to unity), an off-axis density minimum occurs. (This is also referred to as off-axis hollowing.) For $T/T_B < 1-f$ and moderate or high f , the beam core is broader than the plasma current profile, and on-axis hollowing results. (continues)					
20 DISTRIBUTION / AVAILABILITY OF ABSTRACT <input checked="" type="checkbox"/> UNCLASSIFIED-UNLIMITED <input type="checkbox"/> SAME AS RPT <input type="checkbox"/> DTIC USERS			21 ABSTRACT SECURITY CLASSIFICATION UNCLASSIFIED		
22a NAME OF RESPONSIBLE INDIVIDUAL Richard F. Hubbard			22b TELEPHONE (Include Area Code) (202) 767-2927	22c OFFICE SYMBOL Code 4790	

DD Form 1473, JUN 86

Previous editions are obsolete

S/N 0102-LF-014-6603

SECURITY CLASSIFICATION OF THIS PAGE

19. Abstract (continued)

Simulations with the ultrarelativistic SARLAC simulation code exhibit all of these types of equilibria. SARLAC also treats transverse beam distortion arising from the resistive hose instability. Hose instability growth appears to be strongly enhanced when halos are generated.

Keywords - field 18

CONTENTS

I.	INTRODUCTION	1
II.	ANALYTIC EQUILIBRIUM MODELS	4
III.	PARTICLE SIMULATION RESULTS	13
IV.	HOSE INSTABILITY SIMULATIONS	18
V.	CONCLUSIONS	21
	ACKNOWLEDGEMENTS	25
	REFERENCES	26
	DISTRIBUTION LIST	55

Accession For	
NTIS CRA&I	<input checked="" type="checkbox"/>
DTIC TAB	<input type="checkbox"/>
Unannounced	<input type="checkbox"/>
Justification	
By	
Distribution/	
Availability Codes	
Dist	Avail and/or Special
A-1	



HALO FORMATION AND HOLLOWING IN RELATIVISTIC ELECTRON BEAMS

I. INTRODUCTION

Many of the analytical¹⁻⁵ and computational⁵⁻⁷ models used to treat relativistic electron beam propagation in resistive media, such as air, assume that the radial profile of the beam current density $J_b(r)$ has a specified shape. The Bennett profile, which has the form,

$$J_b(r) = \frac{I_b}{\pi a_b^2} \left(1 + \frac{r^2}{a_b^2} \right)^{-2}, \quad (1)$$

is often assumed; it is the correct equilibrium for a beam with no plasma current and an isothermal Maxwellian distribution of perpendicular velocities.^{8,9} An envelope equation¹ is often used to describe the evolution of the scale radius a_b as the beam propagates.

If the beam induces a plasma current $J_p(r)$, the Bennett profile defines the equilibrium only if $J_p(r)$ has the same profile as the beam.³ As revealed in particle simulation code studies,¹⁰⁻¹⁸ compact Bennett-like beam current density profiles generally occur when the plasma current is small or when its profile approximates the local $J_b(r)$. Such codes contain a model for generating the conductivity $\sigma(r)$ as the beam ionizes the air or other gas, and since $J_p = \sigma E_z$ and the axial electric field E_z usually varies slowly with r , the plasma current profile tends to follow the conductivity profile.^{4,5} If the local conductivity is either much narrower or broader than the beam, and if the plasma current I_p is a significant fraction of I_b , large departures from the Bennett profile may occur.¹²

One widely studied example of this occurs when E_z is large enough to cause strong avalanche ionization near the beam axis.^{10,16-20} Joyce and Lampe¹⁰ showed that this process results in violent hollowing, which was first observed in particle simulation codes, and later confirmed experimentally by Ekdahl, et al.²⁰ These experiments also confirmed

theoretical predictions that the instability could be eliminated by limiting the rate of rise of the beam current at the front of the pulse. Although the hollowing process resembles a convective instability, it is more correct to state that the beam's original Bennett-like profile ceases to be an equilibrium, and the beam is seeking a new hollowed equilibrium.

A different process occurs when the conductivity profile is broader than the beam. Simulations of such beams often evolve to a "core and halo" equilibrium in which part of the beam is confined to a small region near the axis while most of the current flows in a halo of much larger radius.¹² Even if the plasma current fraction is small, this process is observed to occur if the transverse beam temperature is too large at injection.¹² Low pressure FX-100 propagation experiments by Ekdahl²¹ may have been the first to exhibit the core-halo phenomenon. Cerenkov data taken during propagation experiments with the RADLAC accelerator sometimes show what appears to be a halo after several meters of propagation.²² Perhaps the strongest evidence for core-halo currents comes from recent x-ray probe measurements made during low pressure propagation experiments on ATA.²³

This paper describes analytical and simulation studies of hollowing and halo formation processes. Analytical models are developed for estimating the equilibrium $J_b(r)$ for an isothermal beam, in the presence of a plasma current with a specified Bennett profile with radius a_p . A purely analytical solution is obtained by iterating about the vector potential generated by a Bennett beam with radius a_{b0} . On-axis hollowing is predicted when $I_b + I_p \ll I_b$ and a_{b0} is somewhat larger than a_p . Large radial wings ("halos") are generated when a_{b0} is small compared with a_p . In extreme cases with $a_{b0} \ll a_p$ and $I_b + I_p \ll I_b$, the beam current profile $J_b(r)$ develops an off-axis minimum. We also show results from a more exact model which numerically integrates Ampere's equation as described by Sharp, et al.;³ it shows qualitatively similar behavior.

Later portions of this paper describe simulations of these phenomena using the axisymmetric code SIMMØ¹⁰ and the 3-D relativistic simulation code SARLAC.¹¹⁻¹³ Since the on-axis hollowing process has been widely studied, most of the results are for cases in which the beam evolves into a core and halo equilibrium. Halo formation is most common in high current beams (> 20 kA) because they produce a large return current fraction and also tend to have broad conductivity profiles because of recombination effects.⁵ Halo formation is further enhanced if the beam temperature or emittance at injection is too large. Mismatched beams of this sort can produce substantial halos even in cases with modest return current fractions.

The last section discusses the effect of halo equilibria on the resistive hose instability. Analytical models⁵ and simulations⁵⁻⁷ which assume a Bennett profile for the beam predict a substantial reduction in hose instability growth as the beam current increases. Simulations with the SARLAC code generally show hose growth decreasing as I_b increases, but much more weakly. The SARLAC simulations suggest that the halo is a destabilizing factor,¹² since it contains particles whose individual betatron frequencies can resonate with low frequency hose modes produced in the expanded head of the beam. Simulations with the VIPER code,⁵ which assumes a Bennett profile for the beam, generally agree well with SARLAC in cases in which the beam remains Bennett-like. However, VIPER predicts much less instability growth than does SARLAC in high current or poorly matched cases which evolve to a core and halo equilibrium. Since halo formation has a strong effect on hose stability, it deserves more experimental study in the future.

II. ANALYTIC EQUILIBRIUM MODELS

A. Assumptions and formalism: Lee,² and Sharp, Lampe and Uhm³ have discussed isothermal equilibria for ultrarelativistic electron beams propagating through dense gases. Conventionally, the beam is assumed to be axisymmetric, and large aspect ratio approximations are made, i.e., $v_{\perp} \ll v_z = c$ for all particles (the "paraxial" approximation), $a_b \partial/\partial z \ll 1$, and $(a_b/c) \partial/\partial t \ll 1$. It is convenient to use r , z , and $\zeta \equiv ct - z$ as independent coordinates instead of r , z , and t ; the quantity ζ is the distance behind the beam head, and is a constant of the motion if $v_z = c$. For beam injection into neutral gas, the gas conductivity $\sigma(r, \zeta, z)$ is due to ionization by the beam itself. It is assumed that σ is large enough to short out radial electric fields within the beam. This is generally well satisfied, except at the very front of the beam and at large radii.^{2,3} The fields E_z and B_{θ} are then derived from A , the z -component of vector potential:

$$E_z = - \partial A / \partial \zeta,$$

$$B_{\theta} = - \partial A / \partial r,$$

and A is determined by Ampere's Law,

$$\frac{1}{r} \frac{\partial}{\partial r} r \frac{\partial A}{\partial r} = - \frac{4\pi}{c} (J_b + J_p) \quad , \quad (2a)$$

while J_p is determined by Ohm's Law,

$$J_p = - \sigma \partial A / \partial \zeta \quad . \quad (2b)$$

We use the conventions that $J_b(r)$ and the total beam current I_b are positive, while $J_p(r)$ and the total plasma current I_p are negative. We also define a (positive constant) return current fraction $f \equiv - I_p / I_b$, a net current $I_n \equiv I_b + I_p$, and a net current fraction $f_n \equiv I_n / I_b \equiv 1 - f$. Ordinarily, $0 < f_n \leq 1$.

In our analytic modeling, we shall assume that $J_b(r, \zeta)$ is ζ -independent and also use the convenient fiction that $J_p(r, \zeta)$ is independent of ζ . In fact, we shall assume a particular form, Eq. (6) below, for $J_p(r)$. Strictly speaking, Eqs. (2) specify J_p and imply that J_p must vary with ζ , but this variation is often quite slow in the main body of the beam, and thus it is quite reasonable to assume J_p is ζ -independent.^{3,5} In the particle simulations discussed in Sec. III, $J_b(r, \zeta)$, $\sigma(r, \zeta)$ and $J_p(r, \zeta)$ are all determined self-consistently, and we do not assume $J_b(\zeta)$ or $J_p(\zeta)$ to be ζ -independent.

In our analytic model, the beam is also assumed to have a Maxwellian distribution of transverse velocities with a uniform temperature T given by^{2,3}

$$T = \frac{1}{2} \gamma m_e \bar{v}_\perp^2 \equiv \frac{1}{2} \gamma m_e c^2 \Delta\theta_t^2 \quad . \quad (3)$$

Here $\bar{v}_\perp = c\Delta\theta_t$ is the transverse thermal velocity of the beam. This isothermal Maxwellian assumption is reasonable for a beam which has passed through a thick scattering foil at injection, or which has been scattered while propagating through uniform gas.⁹ (In the simulations of Sec. III, the isothermal Maxwellian distribution of v_\perp is taken only as an initial condition, and the beam is free to evolve to a different distribution if it wishes.) The radial force on a beam electron is $-e \partial A / \partial r$; thus in Maxwell-Boltzmann equilibrium the beam current density $J_b(r)$ must satisfy

$$J_b(r) = J_{b0} \exp [eA(r)/T] \quad (4)$$

where $J_{b0} = J_b(r=0)$. Equations (2) and (4) are satisfied if $J_p = 0$ and $J_b(r)$ has the Bennett profile defined by (1). In this case, the vector potential is given by

$$A(r) = - \frac{I_b}{c} \ln \left(1 + \frac{r^2}{a_b^2} \right) . \quad (5)$$

B. Iterative Solution for a Non-Bennett Beam: An iterative solution for $J_b(r)$ can be obtained for an isothermal beam with a Bennett plasma current profile given by

$$J_p(r) = \frac{I_p}{na_p^2} \left(1 + \frac{r^2}{a_p^2} \right)^{-2} . \quad (6)$$

The plasma current profile is assumed to be fixed, and an iteration is performed which begins with a zeroth iterate $J_b^{(0)}(r)$ in the form of a Bennett beam profile (1) whose radius a_{b0} can be larger or smaller than a_p . This is used in Eq. (2a) to calculate the zeroth iterate to the vector potential,

$$A^{(0)}(r) = - \frac{I_b}{c} \ln \left(1 + r^2/a_{b0}^2 \right) - \frac{I_p}{c} \ln \left(1 + r^2/a_p^2 \right) . \quad (7)$$

This is substituted into (4) to obtain the next iterate to the equilibrium beam current density,

$$J_b^{(1)}(r) = J_{b0} \left(1 + r^2/a_{b0}^2 \right)^{-2T_B/T} \left(1 + r^2/a_p^2 \right)^{2fT_B/T} . \quad (8)$$

Here $T_B \equiv eI_b/2c$ is the Bennett temperature.

It is important to note that a_{b0} and T are not independent quantities: a_{b0} must be chosen so that J_{b0} satisfies the Bennett pinch condition, which is a necessary but not sufficient condition for equilibrium. (The Bennett pinch condition guarantees that, in a radially averaged sense, the magnetic pinch balances the beam pressure, but it does not guarantee that pressure balance holds at each radial location.) This condition is

$$T = eI_e/2c, \quad (9a)$$

where the "effective current"^{1,4,5} I_e is defined by

$$I_e \equiv 2I_b^{-1} \int_0^{\infty} dr 2\pi r J_b^{(o)}(r) I_n^{(o)}(r), \quad (9b)$$

and for the particular case where $J_b(r)$ and $J_p(r)$ are given by Eqs. (1) and (6),

$$\begin{aligned} I_e &= 2I_b^{-1} \int_0^{\infty} dr 2\pi r \frac{I_b}{\pi a_{bo}^2} \frac{1}{(1 + r^2/a_{bo}^2)^2} \left(\frac{I_b r^2/a_{bo}^2}{1 + r^2/a_{bo}^2} + \frac{I_p r^2/a_p^2}{1 + r^2/a_p^2} \right) \\ &= I_b \left[1 - \frac{2fa_{bo}^2/a_p^2}{(a_{bo}^2/a_p^2)^{-1}} \left(1 - \frac{\ln(a_{bo}^2/a_p^2)}{(a_{bo}^2/a_p^2)^{-1}} \right) \right]. \end{aligned} \quad (9c)$$

Here $I_n^{(o)}(r)$ is the net current enclosed within radius r . I_e is essentially a measure of the pinch-effectiveness of the net current contained within the beam, whereas $I_n \equiv I_b + I_p$ is the total net current out to $r = \infty$ (or to the walls). Thus, $I_e > I_n$ if $a_{bo} < a_p$ (so that much of the plasma return current is outside the beam). $I_e \rightarrow I_b$ in the limit $a_{bo}/a_p \rightarrow 0$. Conversely, $I_e < I_n$ if $a_{bo} > a_p$, and $I_e \rightarrow I_b + 2I_p$ when $a_{bo}/a_p \rightarrow \infty$. This is because current elements that are entirely within the beam are twice as effective in determining the average pinch force. Thus one may regard Eqs. (9) as a relation determining a_{bo} as a function of T and f , or alternatively defining T as a function of a_{bo}/a_p and f . We note that increasing T corresponds to reducing a_{bo} (in order to minimize the plasma return current contained within the beam). This is at odds with intuition, since one usually thinks of increased beam transverse temperature as leading, in a dynamic sense, to expansion. We note that no equilibrium is

possible [(9) has no solution] if $T > T_B$ or $T < T_B(1-2f)$. In the former case, the beam is too hot to be pinched even by the unshielded beam pinch force, whereas in the latter case the beam is too cool to support itself even against the weakened pinch force corresponding to return current flow entirely in a narrow region on-axis. Figure 1 plots T versus a_{bo}/a_p for a series of cases with $f_n = 0.15$ and $f_n = 0.8$.

Equations (8) and (9) give a great deal of detailed information about the beam profiles $J_b(r)$. This information is summarized in Table I and will be discussed in this subsection and the next.

In cases with small return currents, the equilibrium is expected to remain close to the Bennett profile, which is the exact solution if $I_p = 0$. Figure 2 plots profiles of $J_b^{(1)}(r)/J_b^{(1)}(r=0)$ from (8) using $a_{bo}/a_p = 0.4, 0.7, 1.0,$ and $1.15,$ and T calculated from (9). The net current fraction is $f_n = 0.8$. In all cases, $J_b^{(1)}(r)$ is close to the r^{-4} scaling expected for a Bennett beam at large radius; no hollowing or halo formation is observed.

Next we consider cases in which the return current is substantial, beginning with the regime $a_{bo}/a_p < 1$, for which $1-f < T/T_B < 1$. Using Eqs. (9), this condition can also be written in the equivalent form $f_n < f_e$, which indicates directly that in some average sense the beam is narrower than the $J_p(r)$ profile. Here, Eq. (8) shows that in the central part of the beam, $J_b^{(1)}(r)$ scales as $(1 + r^2/a_{bo}^2)^{-p}$ with $p > 2$, and thus has a steeper fall-off than a Bennett. However, $J_b^{(1)}(r)$ scales as $r^{-p'}$, with $p' < 4$, for large r . Thus, there is a tightly pinched central core surrounded by an extended lower-density halo. It is interesting to note that as T increases above $(1-f)T_B$, the core radius decreases (as predicted above in the discussion of a_{bo}), but progressively more of the current is carried in the halo, whose radius increases. Thus, the half radius (defined as the radius within which half the beam current flows) typically increases as a function of T .

Figure 3 shows a series of calculations for a case with a strong plasma return current, $f_n = 0.15$. The beam equilibrium for $a_{bo}/a_p = 0.4$ exhibits core and halo behavior: $J_b^{(1)}(r)$ drops by three orders of magnitude between $0 \leq r/a_p \leq 3$, but only by a factor of 3 as r/a_p increases from 3 to 10.

When $a_{bo}/a_p = 1$, it follows that $T = T_B(1-f)$ and Eq. (8) shows that the Bennett profile is recovered. This is shown as the second curve in Fig. 3.

For $a_{bo}/a_p > 1$, Eq. (8) gives two subcases. If $J_{bo}(0) + J_p(0) < 0$, the profile $J_b^{(1)}(r)$ is hollowed on-axis, i.e., has a minimum on-axis and a single maximum somewhere off-axis. This can be seen by differentiating Eq. (8); extrema are found at $r = 0$ and at

$$r^2 = -\pi \frac{J_p(0) + J_b^{(o)}(0)}{I_b + I_p} a_{bo}^2 a_p^2 . \quad (10)$$

One and only one extremum for $r^2 > 0$ exists if and only if $-J_p(0) > J_b^{(o)}(0)$, which can occur only if the beam is wider than the return current profile. This situation is shown in the top curve of Fig. 3, where $a_{bo}/a_p = 1.15$ and $f_n = 0.15$. If, on the other hand, $a_{bo}/a_p > 1$ but $J_b^{(o)}(0) + J_p(0) > 0$, then $J_b^{(1)}(r)$ is flattened near $r = 0$, but is not hollowed.

The equilibria shown in Fig. 3 resemble the "generalized Bennett" equilibria obtained by Benford, Book, and Sudan.²⁴ However, their generalized Bennett $J_b(r)$ is zero on axis for all cases which exhibit on axis hollowing, and their cases which resemble core/halo profiles have infinite current density at $r = 0$.

Finally, we consider the occurrence of off-axis hollowing, which is defined as having a $J_b(r)$ profile that has a maximum on-axis, a minimum somewhere off-axis, and then a second maximum further out radially. Since Eq. (8) gives, at most, one off-axis extremum, off-axis hollowing is not predicted by the first iteration $J_b^{(1)}(r)$. However, a second iteration does predict off-axis hollowing under conditions where a_{bo}/a_p is small and f_n is small. We can see this by going part way towards a next iteration. In equilibrium, the beam satisfies the pressure balance condition

$$\frac{1}{c} \vec{J}_{bz} \times \vec{B}_\theta = - \frac{\partial P}{\partial r} = - \frac{\partial}{\partial r} \left(\frac{J_b^T}{ec} \right) \quad (11)$$

Hollowing occurs when there is a region where $\partial J_b / \partial r > 0$. According to (11), this requires that $B_\theta(r)$ change sign, which is equivalent to requiring that the enclosed net current $I_n(r)$ change sign. To first order, the net current density $J_n^{(1)}(r) = J_b^{(1)}(r) + J_p(r)$ is given by (6) and (8), and the enclosed net current is

$$\begin{aligned} I_n^{(1)}(r) &= I_b^{(1)}(r) + I_p(r) \\ &= 2\pi \int_0^r dr' r' \left[1 + \left(\frac{r'}{a_p} \right)^2 \right]^{2fT_B/T} \left[1 + \left(\frac{r'}{a_{bo}} \right)^2 \right]^{-2T_B/T} + \frac{I_p r^2 / a_p^2}{1 + r^2 / a_p^2} \end{aligned} \quad (12)$$

The integral in (12) can be evaluated numerically.

Figure 4 plots the enclosed currents $I_b^{(1)}(r)$, $I_p(r)$ and $I_n^{(1)}(r)$ for a case with $a_{bo}/a_p = 0.8$ and $f_n = 0.15$. The enclosed net current remains positive everywhere, so this case is expected to show core and halo behavior. In Fig. 5, a_{bo}/a_p has been reduced to 0.4, and there is a significant region where $I_n^{(1)}(r)$ is negative. This example would thus show off-axis hollowing in the next iteration.

C. Numerical Integration of Ampere's Equation: The iterative procedure offers considerable insight into the hollowing and halo formation processes, but one or two iterations does not necessarily yield a quantitatively accurate calculation of $J_b(r)$ when $J_b(r)$ is very different from the Bennett profile which is the starting point for the iteration. In the present section we continue to assume that $J_p(r)$ has the Bennett shape (6), but we calculate $J_b(r)$ directly by numerically integrating Ampere's law (2a) and the Boltzmann equilibrium condition (4) together. This method was employed by Sharp, et al.,³ to construct equilibria for hose instability calculations. Values for a_p , $J_p(0)$, $J_b(0)$ and T are chosen, and (2a) is integrated numerically from $r = 0$ to $r = \infty$, using (4) to generate $J_b(r)$. We then calculate I_b by integrating $J_b(r)$:

$$I_b = 2\pi \int_0^{\infty} dr r J_b(r) \quad , \quad (13)$$

and $f \equiv -I_p/I_b$ or $f_n \equiv 1-f$ are thus specified. The procedure can be repeated, adjusting the initial value of $J_b(0)/J_p(0)$, to converge to a desired value of f , or alternatively to a desired ratio of a_p to some characteristic beam radius.

Figures 6-8 show examples in which $f_n < T/T_B$, and thus the core of the beam has a narrower profile than $J_p(r)$ and beam profiles of core/halo type are expected. In Fig. 6, $f_n = 0.47$ and $T/T_B = 0.6$; because the return current is not too large $J_b(r)$ is close to the Bennett profile, with a weak halo. In Fig. 7, $T/T_B = 0.2$ and there is a stronger return current, $f_n = 0.18$. This beam more clearly exhibits core and halo behavior, as expected from the simple iterative theory of Sec. IIB. However, the present solution (in contrast to the more approximate result shown in Fig. 2) shows that the halo does not extend indefinitely, but rather $J_b(r)$

falls off rapidly for $r \geq 2 a_p$. This type of behavior is seen in the simulations reported in Sec. III. In Fig. 8, $T/T_B = 0.1$ and the return current is still stronger, $f_n = 0.083$. This example exhibits off-axis hollowing. Figure 9 shows a case in which there is strong return current, $f_n = 0.08$, and $T/T_B = 0.05 < f_n$. Thus $J_p(r)$ has a narrower profile than the beam, and in fact $-J_p(0) > J_b(0)$. The beam exhibits on-axis hollowing, as expected.

III. PARTICLE SIMULATION RESULTS

A. Model Descriptions: Particle simulations have been widely used to study relativistic electron beam propagation.⁹⁻¹⁷ Most of the results presented here were obtained with SARLAC, an ultrarelativistic 3-D particle simulation.¹¹⁻¹³ It differs from conventional plasma simulations in that $v_{\perp} \ll v_z = c$, so particles remain at the same distance ζ from the beam head, and field and conductivity equations are integrated in ζ . The field solver is based on the Lee field equations^{5,25} for a relativistic, paraxial beam. The conductivity equations employ a variable temperature model²⁶ and include beam impact ionization, avalanche, and recombination. The beam is injected with a Bennett profile with radius a_0 and a constant temperature T_0 . The SARLAC code is described in more detail elsewhere.^{11,13}

Results on on-axis hollowing were obtained with SIMMØ, an axisymmetric particle simulation.¹⁰ Except for the axisymmetric assumption, the code is similar to SARLAC.

B. Overview of SARLAC Simulations: Eight simulations were performed with the SARLAC code using various values of beam current and beam transverse temperature. These simulations are described in Table II. The high current (≥ 100 kA) cases produced large return currents and broad conductivity profiles (due to recombination effects and beam tapering). In agreement with the theory presented in Sec. II, these cases show core and halo behavior when the initial transverse temperature T_0 is large, i.e.,

$$f_m \equiv T_0/T_B > f_n . \quad (14)$$

In simulation parlance, f_m defined in (14) is called the "matching current fraction" -- the beam as injected would be in a Bennett-like equilibrium if the net current fraction f_n turned out to be equal to f_m . If the "matching

current" is larger than the self-consistently determined net current, that means that the beam is "overpressured" - i.e., too hot - at injection. Halos were produced in a 10 kA case when f_m was very large, even though the return current fraction was modest. In one extreme case with $I_b = 500$ kA, off-axis hollowing was observed.

To quantify the degree of halo formation, the radius $a_{1/2}$ enclosing half of the beam current was compared with a_{core} , a Bennett radius fit to the beam core. For a Bennett-like beam, $a_{1/2} \approx a_{\text{core}}$, while $a_{1/2} \geq 2 a_B$ for a beam with a strong halo. The radius measurements were taken at $\zeta = 80 a_0$ and $z = 240 a_0$ where a_0 was the Bennett radius of the injected beam.

C. Bennett-like Examples: Case 1 is a 10 kA beam with $f_m = 0.5$, a temperature close to that required for a well-matched injection. Since $I_p/I_b \approx 0.5$ for this case, the beam should remain Bennett-like. Figure 10 plots $J_b(r)$ and $J_n(r) \equiv J_b(r) + J_p(r)$ at $\zeta = 80$ cm and $z = 240$ cm. The profiles are similar in shape and there is no evidence for a halo. Figure 11 compares $J_b(r)$ with a Bennett fit; the fit is excellent even out to large radii where $J_b(r)$ has dropped by several orders of magnitude. Figure 12 plots the pinch force per beam electron $F_r(r)$ for this case. It shows the expected smooth behavior for a Bennett-like beam.

Figure 13 plots the x and y positions of a subset of individual simulation particles vs ζ after the beam has propagated to $z = 320$ cm. The beam flares at the head because it takes time for the net current and pinch force to build up.⁴ The beam is clearly well-pinchd, and hose instability distortions are barely visible.

A 100 kA beam typically produces a broad conductivity profile and a small net current ($I_n \sim 0.1 - 0.2 I_b$), conditions which typically lead to a core/halo equilibrium. SARC simulations of 100 kA beams reached Bennett-like equilibria only when the head of the beam was expanded and cooled prior to injection into the gas, in order to improve the match throughout the beam. In cases 6 and 7, the beam was injected with a tapered radius

$$a(\zeta, z=0) = (\zeta_r/\zeta)^{1/2} a_0, \quad (15)$$

but the emittance at injection, which is proportional to $a(\zeta, 0)(f_m(\zeta, 0))^{1/2}$, was constant as a function of ζ . For $f_m = 0.2$ (case 7), the beam remains Bennett-like, as shown in Fig. 14. For $f_m = 0.4$ (case 6), modest departures (core/halo) from the initial Bennett profile occur.

D. Core and Halo Examples: Case 4 is a 100 kA beam with $f_m = 0.4$, a relatively high temperature for a beam with such a small net current fraction. Figure 15 plots $J_b(r)$ and $J_n(r)$, showing the presence of a halo between $r = 5$ cm and $r = 15$ cm. The beam is well represented by a Bennett out to $r = 5$ cm. Since $a_{1/2} > 3a_{\text{core}}$ (Table II), this may be considered a strong halo case. The core, whose radius $a_{\text{core}} = 1.1 a_0 = 3.3$ cm, carries only about 15% of the total current. Most of the beam is contained in the halo. The net current density $J_n(r)$ is actually negative just inside the halo. This leads to a local off-axis minimum in $|F_r(r)|$, as seen in Fig. 16. This tends to push particles from the core to the halo. The halo is clearly seen in the particle plots shown in Fig. 17, along with the high density core. Consistent with Fig. 15, the halo has a relatively well-defined edge. Codes such as VIPER, which impose a Bennett profile on the beam and use an envelope equation to estimate the beam radius, predict that

the beam radius should taper back from the beam head due to the gradual build-up of the effective current defined in (9). The behavior seen in Fig. 17 is much different. The implications of this for hose instability are discussed in Sec. IV.

Strong halo formation of a similar nature is seen in Case 3 ($I_b = 50$ kA, $f_m = 0.4$). In Case 5 ($I_b = 100$ kA) f_m was reduced from 0.4 to 0.2 in order to produce a better match at injection; only mild halo formation was observed in this case.

We have also observed halo formation in lower current beams when the initial temperature or emittance is poorly matched. Case 2 is such an example; it is identical to the 10 kA Case 1 except that $f_m = 1.5$. As seen in Fig. 18, a halo forms at $r = 2$ cm, and the Bennett core carries only about 25% of the total current. From Table II, $a_{1/2}/a_{\text{core}} = 2.5$ for this case. We believe that this case is qualitatively different from the high-current cases discussed in this paper; there is not enough plasma return current to account for the halo through the mechanism discussed in Sec. II. In this case, the evolution to a core/halo equilibrium appears to be due to a strong departure from Maxwell-Boltzmann equilibrium. This beam is injected with a transverse pressure that far exceeds the pinch force, and the resulting non-adiabatic behavior (large-amplitude bounces) heats some electrons far more than others and introduces structure in phase space. We believe that this type of behavior may be a significant feature of some beam propagation experiments, and intend to explore it further in future work.

E. Off-Axis Hollowing Cases: Figure 8 indicates that off-axis hollowing can occur if $f_n \equiv I_n/I_b$ is sufficiently small. Small f_n is associated with very high beam current. Case 8 is similar to Case 2 but with $I_b = 500$ kA

and $f_m = 0.2$. A plot of $J_b(r)$ at $z = 1200$ cm and $\zeta = 480$ cm (Fig. 19) reveals an off-axis minimum at $r = 40$ cm. Again the core contains only a small fraction of the current. An off-axis minimum is not observable in plots of the x and y positions of simulation particles, so Fig. 20 also plots the radial position r_i of simulation particles at $z = 200 a_0 = 1200$ cm. The core has a relatively sharp edge, followed by a gap in particles corresponding to the off-axis minimum.

The conditions to produce off-axis hollowing by a beam injected into an initially neutral gas are well beyond present technology. However, our axisymmetric simulations using the SIMMØ particle code indicate that off-axis hollowing can occur when a lower current beam is injected into a highly conducting channel, which carries a current $I_n \sim 0.1 I_b$ and is somewhat broader than the beam. Such conditions can occur when a beam is injected into a laser-guided electric discharge. Keeley²⁷ has observed similar behavior using a fluid beam simulation code.

F. On-Axis Hollowing: As seen in previous theoretical and experimental studies, on-axis hollowing usually causes violent disruption of the propagating beam.^{10,15-18} The disruptive instability is driven by enhancement of avalanche ionization near the beam axis. An example of on-axis hollowing which remains quiescent and near equilibrium is shown in Fig. 21. The simulation was performed with the SIMMØ code for a 10 kA beam propagating in a reduced density channel with density $\rho(r=0) = 0.1$ atm. The channel radius a_c is twice the beam radius, and $\rho(r \gg a_c)$ approaches 1 atm. The surface plot of $J_b(r, \zeta)$, at $z = 800$ cm, exhibits the mild on-axis hollowing. Figure 22 plots the radius $a_{1/2}(\zeta, z)$. Although some oscillations are present, the beam propagates without disruption.

IV. HOSE INSTABILITY SIMULATIONS

A. Introduction: The resistive hose instability can seriously disrupt propagation of relativistic electron beams.^{2,3,5-7} However, it is sometimes possible to avoid severe disruption by taking advantage of the convective nature of the instability. An initial excitation convects backward in the beam, growing as it convects. Thus the hose amplitude, at a given point ζ in the beam, initially grows and then reaches a maximum and subsequently decays as the disturbance convects past; this is known as convective saturation. The linear theory of the instability has been developed in Refs. 2, 3 and 5.

SARLAC was primarily intended for studying this instability. It is less restrictive than older phenomenological codes such as VIPER,⁵ EMPULSE,⁶ and PHLAP⁷ in three ways: First, SARLAC can follow the instability into the large-amplitude regime, whereas the older codes linearize in hose amplitude (compared to beam radius). Second, SARLAC follows exact particle trajectories, whereas the older codes use the spread mass² or multicomponent³ beam dynamics models. However, careful studies⁵ have shown that these models are quite accurate, at least for small amplitude hose. Third, the older codes impose a Bennett radial profile on the beam, but SARLAC allows the beam profile $J_b(r)$ to change its shape self-consistently. For our purposes here, this is the most important difference between SARLAC and the older codes. In this section, we examine the hose instability behavior of the cases described in the previous section and compare the SARLAC results with those obtained from VIPER.

B. Bennett-like Cases: For cases in which the beam remains Bennett-like, we expect VIPER and SARLAC to predict comparable hose growth in the linear regime. Figure 23 plots the displacement $\bar{X}(z)$ of the beam centroid for

Case 1, which is a Bennett-like 10 kA beam. SARLAC results are shown for $\zeta = 40, 80,$ and 160 cm, and a VIPER result for $\zeta = 160$ cm. (The VIPER amplitudes are normalized to $X_0 = 10^{-2}$ cm, the amplitude of the initial SARLAC perturbation). As expected, the two codes are in substantial agreement. This is also shown in line 1 of Table III, which compares the SARLAC and VIPER values for $\ln(\bar{X}/X_0)$ evaluated at $\zeta = 80 a_0$ and $z \leq 400 a_0$. Once the beam propagates a short distance, the radius $a_{1/2}(\zeta)$ in the region of strong hose growth is almost constant. This is seen in Fig. 24.

C. Core and Halo Examples: In all cases where there is a halo, SARLAC predicts more hose growth than VIPER. In Case 5, only mild halo formation is seen in the SARLAC simulation, and SARLAC shows 5.9 e-foldings of growth, a mild enhancement compared to the 4.4 e-foldings shown by VIPER. The high current Case 4 exhibits strong halo formation. Figure 25 plots $\bar{X}(z)$ for this case. The three SARLAC curves at $\zeta = 120, 240,$ and 360 cm show substantial instability growth, which is also apparent in the particle plots shown in Fig. 26. [This plot is at $z = 1200$ cm which was the end of the simulation run. At $z = 720$ cm (Fig. 17), the beam does not yet exhibit large amplitude hose.] However, the normalized amplitude from VIPER at $\zeta = 360$ cm shows very little growth. Indeed, Table III shows 3.9 e-folds of growth for SARLAC, but only 0.8 e-folds for VIPER. Case 2, a 10 kA beam which exhibits strong halo formation, also shows a factor of 2 more instability e-foldings with SARLAC than with VIPER.

D. Discussion: It appears to be generally true that the presence of a halo exacerbates hose instability, as compared to the same case treated with a model that artificially imposes a Bennett profile. We believe this

is true because $J_b(r, \zeta)$ is nearly constant in both r and ζ within the halos seen in SARLAC simulations, and thus, there is much less variation in betatron frequency among beam particles, as compared to beams with Bennett profiles. It has been known for many years^{2,3} that betatron frequency spread greatly reduces the hose growth rate and leads to convective saturation. Particularly in the case of high-current beams ($I_b \gg 10$ kA), envelope code simulations (which impose a Bennett profile) typically show a gradual tapering of the half-radius $a_{1/2}(\zeta)$, as a function of ζ , as illustrated in the VIPER simulation of Case 4 in Fig. 27. This tapering leads to betatron-frequency variation, and is a stabilizing feature. The SARLAC simulation of the same case (Fig. 27) shows much less variation in $a_{1/2}$ within the beam body.

It should be noted that the point of Table III is to compare SARLAC to VIPER hose growth for each individual case. The comparison of hose growth among different cases is not meaningful, without considering many factors that have not been discussed here and that are different for the various cases, e.g., propagation distances z must be scaled to the betatron wavelength, locations ζ (relative to the beam head) must be scaled to "dipole decay lengths" $\pi \sigma a_{1/2}^2 / 2c$, and the variation $a_{1/2}(\zeta)$ must be taken into account.

V. CONCLUSIONS

Particle simulations of propagating relativistic electron beams with large return current fractions often exhibit large departures from the compact Bennett or Gaussian profiles usually assumed in theoretical calculations. Beams with narrow return current profiles may show on-axis hollowing, while those with broad return current profiles may form a core and halo or an off-axis minimum in $J_b(r)$. All of these features can be reproduced in analytic models which calculate an equilibrium $J_b(r)$ compatible with Ampere's equation.

Beams which evolve to highly non-Bennett radial profiles may be strongly destabilized. A beam with a narrow conductivity profile and an equilibrium with an on-axis minimum is likely to be disrupted by the axisymmetric hollowing instability. High return current beams with broad conductivity profiles may develop a halo which can strongly enhance hose instability disruption. Since most of the beam usually resides in the halo in these cases, the presence of a small current in a tight core may be of little consequence. The important role of the $J_b(r)$ profile in determining beam stability may warrant more careful experimental examination of the phenomena.

Table I. A summary of the analytic model for beam equilibrium.

f	a_{bo}/a_p	T/T_B	Form of profile $J_b(r)$
0	-	1	Bennett
close to 0	any value	close to 1	Bennett-like
		> 1	no solution
moderate	< 1	$1-f < T/T_B < 1$	core/halo
close to 1	< 1	$1-f < T/T_B < 1$	off-axis hollowed
any value	1	$1-f$	Bennett
$> a_p^2/a_{bo}^2$	> 1	$1-2f < T/T_B < 1-f$	hollowed on axis
$< a_p^2/a_{bo}^2$	> 1	$1-2f < T/T_B < 1-f$	flattened on axis
		< $1-2f$	no solution

Table II. This table summarizes the initial conditions and the type of equilibrium attained in eight SARCAC simulations. In all cases, the beam electrons initially have relativistic factor $\gamma = 100$, the gas is air at standard temperature and pressure, the simulation region is terminated by a perfectly conducting wall at $r = 81 a_0$, and the beam current $I_b(\zeta)$ rises to its full value over a rise length $\zeta_r = 120 a_0$. Those cases designated "pencil beam" are injected with uniform emittance and radius a_0 , while those designated "tapered" are injected with uniform emittance, but with a tapered radius $a(\zeta)/a_0 = (\zeta_r/\zeta)^{1/2}$, and $T(\zeta) \sim [a(\zeta)]^{-1/2}$. $a_{1/2}$ is the "half-radius" of the beam, while a_{core} is a Bennett radius fit to the central part of the beam. The quantities f_n , $a_{1/2}$ and a_{core} are evaluated at $\zeta = 80 a_0$ and $z = 240 a_0$. The matching current fraction f_m is defined in (14).

Case	I_b (kA)	a_0 (cm)	f_m	f_n	$a_{1/2}/a_0$	a_{core}/a_0	Description
1	10	1 (pencil)	0.5	0.53	1.2	1.1	Bennett-like
2	10	1 (pencil)	1.5	0.58	3.5	1.4	Strong halo
3	50	3 (pencil)	0.4	0.21	3.1	1.5	Strong halo
4	100	3 (pencil)	0.4	0.22	3.5	1.1	Strong halo
5	100	3 (pencil)	0.2	0.16	1.6	0.9	Moderate halo
6	100	3 (tapered)	0.4	0.17	2.4	1.7	Moderate halo
7	100	3 (tapered)	0.2	0.13	1.5	1.8	Bennett-like
8	500	6 (pencil)	0.2	0.04	3.2	1.2	Off-axis hollowed

Table III. Hose instability growth, for four of the cases described in Table 2. \bar{X} is the largest hose amplitude seen at $\zeta = 80 a_0$ for $z \leq 400 a_0$, while X_0 is the initial hose amplitude.

Case	I_b (kA)	Description	SARLAC $\ln(\bar{X}/X_0)$	VIPER $\ln(\bar{X}/X_0)$
1	10	Bennett-like	5.4	4.9
2	10	Strong halo	0.6	0.3
4	100	Strong halo	3.9	0.8
5	100	Moderate halo	5.9	4.4

Acknowledgments

We wish to acknowledge discussions with Drs. R. Fernsler, W. Sharp, W. Fawley, R. L. Feinstein, B. Hui, C.A. Ekdahl, K. Brueckner, D. Keeley, B. Godfrey and C. Frost. We also thank Mr. P. Boris for assistance in preparing the figures.

This work was supported by the Defense Advanced Research Projects Agency under ARPA Order No. 4395, Amendment No. 69, and monitored by the Naval Surface Warfare Center.

References

1. E. P. Lee and R. K. Cooper, Part. Accel. 7, 83 (1976).
2. E. P. Lee, Phys. Fluids 21, 1327 (1978).
3. W. Sharp, M. Lampe, and H. Uhm, Phys. Fluids 25, 1456 (1982).
4. W. Sharp and M. Lampe, Phys. Fluids 23, 2383 (1980).
5. M. Lampe, W. Sharp, R. Hubbard, E. Lee, and R. Briggs, Phys. Fluids 27, 2971 (1984).
6. E. P. Lee, F. W. Chambers, L. L. Lodestro, and S. S. Yu, in Proceedings of the Second International Conference on High Power Electron and Ion Beam Research and Technology, Cornell University, 1977, p. 381; W. Fawley and W. Sharp (private communication).
7. R. L. Feinstein, D. A. Keeley, E. R. Parkinson, and W. Rienstra, Science Applications International Corp., SAIC-U-74-PA-DOE (1984).
8. W. H. Bennett, Phys. Rev. 45, 890 (1934).
9. E. P. Lee, Phys. Fluids 19, 60 (1976).
10. G. Joyce and M. Lampe, Phys. Fluids 26, 3377 (1983).
11. G. Joyce, R. F. Hubbard, M. Lampe, and S. P. Slinker, NRL Memorandum Report 6140, also submitted to J. Comp. Phys.
12. R. F. Hubbard, S. P. Slinker, G. Joyce and M. Lampe, Bull. Am. Phys. Soc. 31, 1429 (1986).
13. R. F. Fernsler, R. F. Hubbard, B. Hui, G. Joyce, M. Lampe, and Y. Y. Lau, Phys. Fluids 29, 3056 (1986).
14. J. R. Freeman, J. W. Poukey, J. S. Wagner, and R. S. Coats, J. Appl. Phys. 59, 725 (1986).
15. B. B. Godfrey and D. Welch, Mission Research Corp., AMRC-R-966 (1987).
16. F. W. Chambers, J. A. Masamitsu, and E. P. Lee, Lawrence Livermore National Laboratory, UCID-19494 (1982).
17. B. B. Godfrey, Phys. Fluids 30, 570 (1987); B. B. Godfrey, Phys. Fluids 30, 575 (1987).
18. K. Brueckner (private communication).
19. M. Lampe and G. Joyce, Phys. Fluids 26, 3371 (1983).
20. C. A. Ekdahl, J. R. Freeman, G. J. Leifeste, R. B. Miller, W. B. Styger, and B. B. Godfrey, Phys. Rev. Lett. 55, 935 (1985).

21. C. A. Ekdahl, Mission Research Corporation, AMRC-R-352 (1982).
22. C. Frost (private communication).
23. W. Fawley, K. Struve and F. Chambers, Bull. Am. Phys. Soc., April 1988 (in press).
24. G. Benford, D. L. Book and R. N. Sudan, Phys. Fluids 13, 2621 (1970).
25. E. P. Lee, Lawrence Livermore National Laboratory, UCID-17286 (1976); B. Hui and M. Lampe, J. Comp. Phys. 55, 328 (1984).
26. S. P. Slinker, R. F. Hubbard, and M. Lampe, NRL Memo Report 6004 (1987); J. Appl. Phys. 62, 1171 (1987).
27. D. Keeley (private communication).

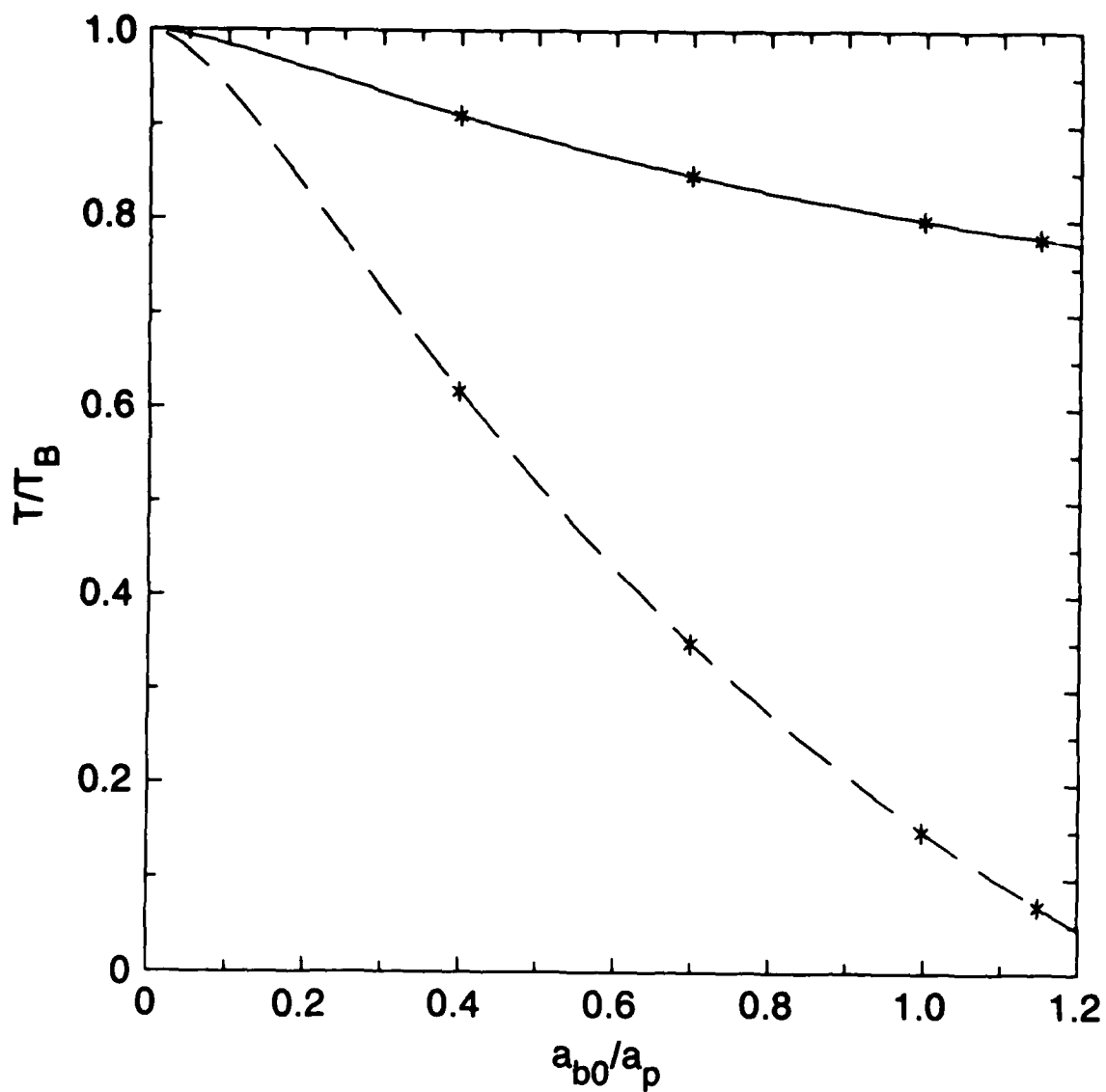


Fig. 1 Equilibrium value of T/T_B versus the nominal beam radius ratio a_{b0}/a_p . The solid line is for $f_n = 0.8$, and the dashed line is for $f_n = 0.15$. The asterisks correspond to the cases plotted in Figs. 2 and 3.

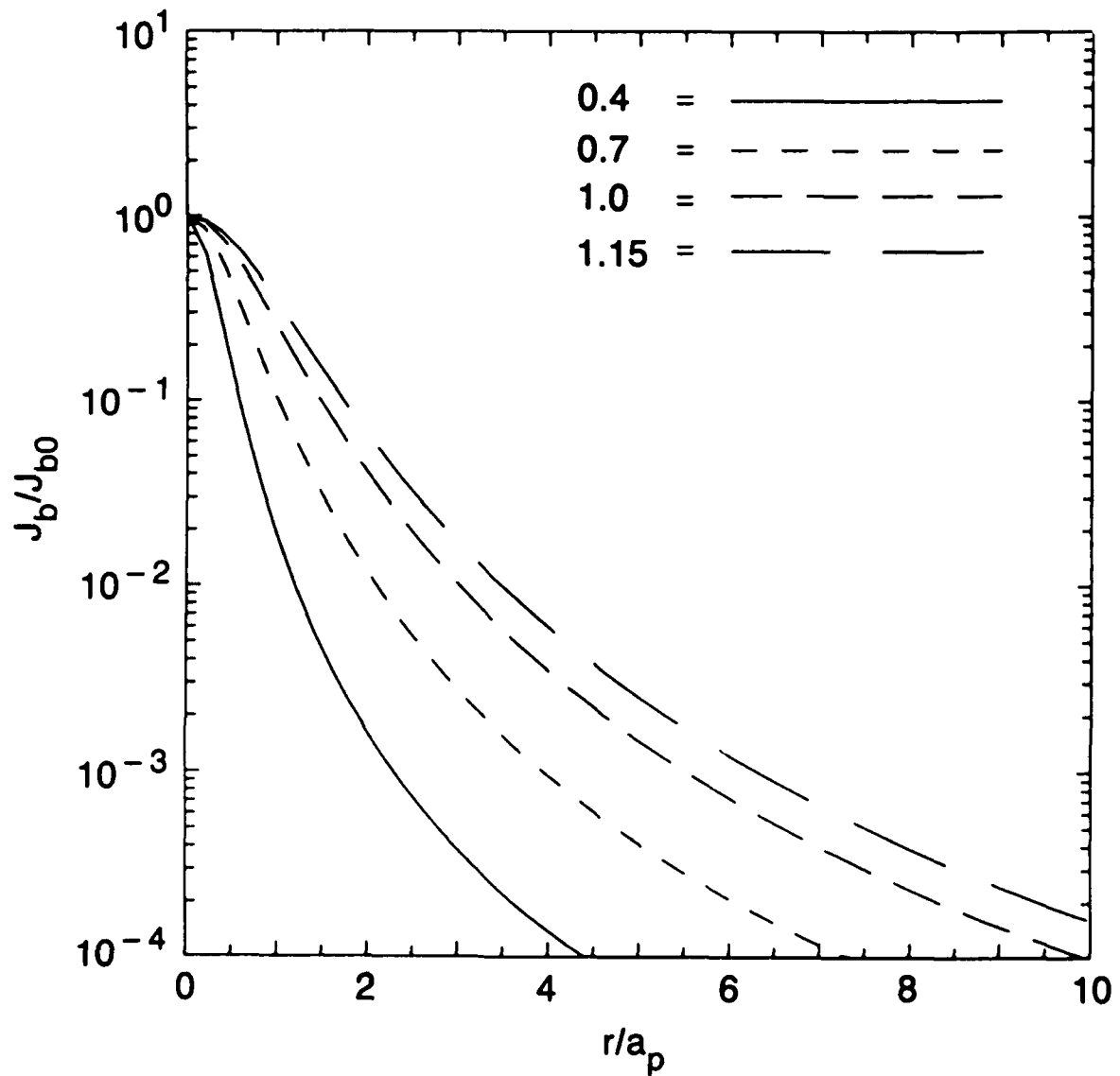


Fig. 2 Equilibrium beam current density $J_b^{(1)}(r)$ calculated from (8) for a beam with net current fraction $f_n = 0.8$. The curves are for nominal beam radius $a_{b0} = 0.4, 0.7, 1.0,$ and 1.15 (normalized to the plasma current radius a_p). The radial profiles are all Bennett-like.

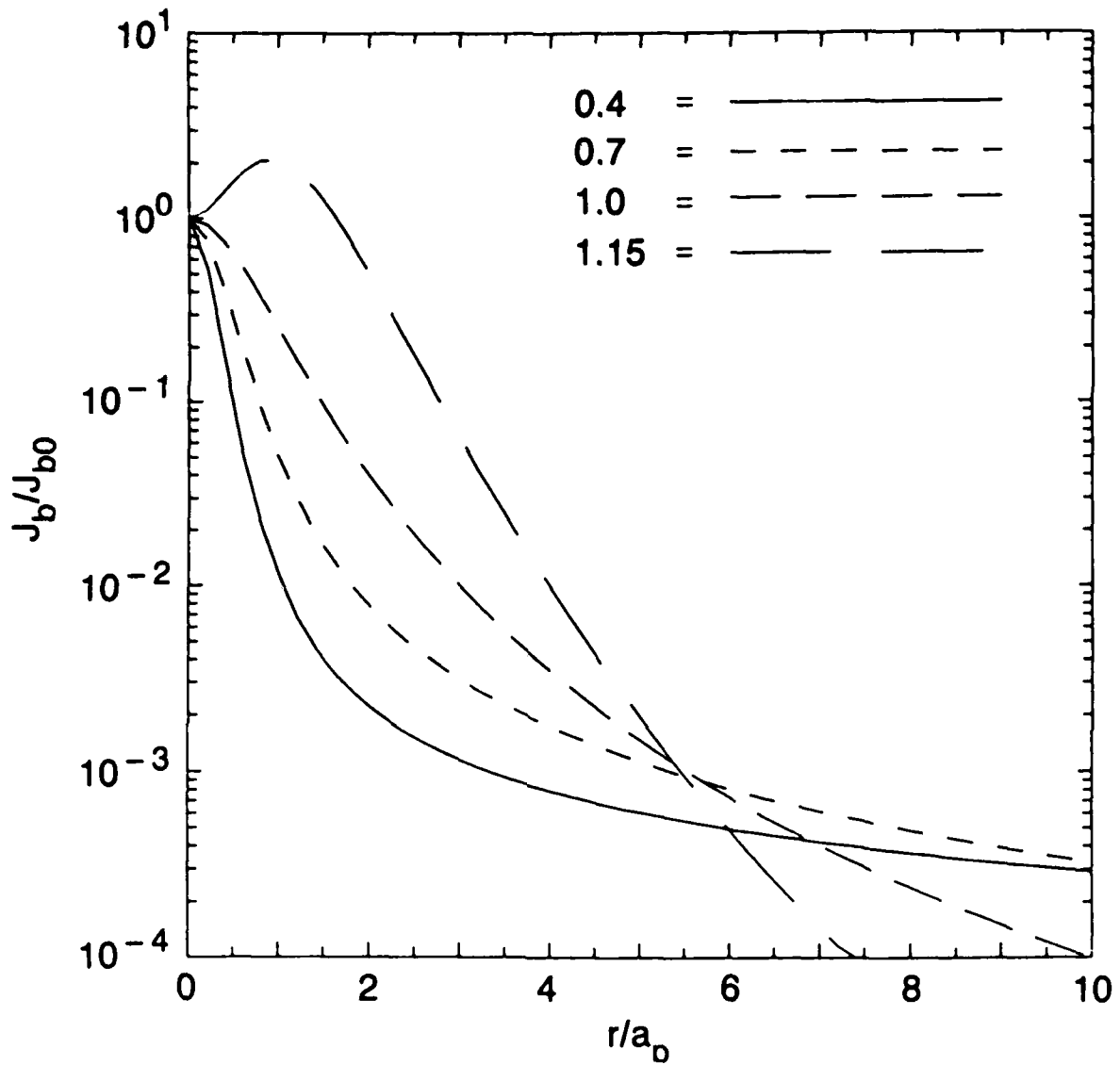


Fig. 3 Equilibrium $J_b^{(1)}(r)$ for a beam with $f_n = 0.15$. For $a_{b0}/a_p = 0.4$ and 0.7 , the current density falls off slowly with r for $r \gg a_{b0}$, thus exhibiting core and halo behavior. For $a_{b0}/a_p = 1.15$, the beam exhibits on-axis hollowing.

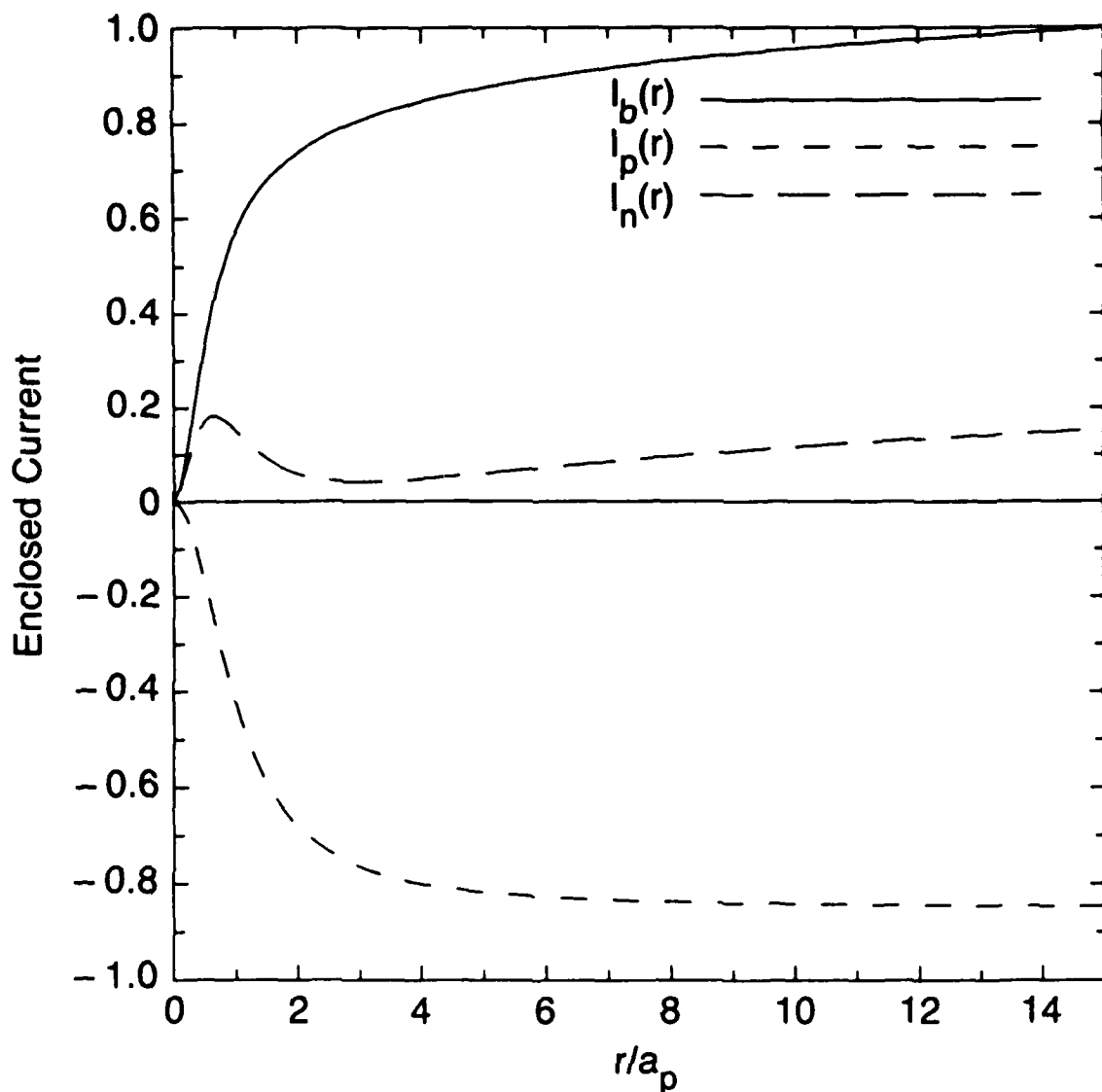


Fig. 4 Enclosed currents $I_b^{(1)}(r)$, $I_p(r)$ and $I_n^{(1)}(r)$ versus radius r/a_p , normalized to $I_b(r = 15 a_p)$. Results are calculated from (12) assuming $f_n = 0.15$ and $a_{bo}/a_p = 0.8$. Since $I_n^{(1)}$ is positive but shows a pronounced dip, this beam exhibits core and halo behavior.

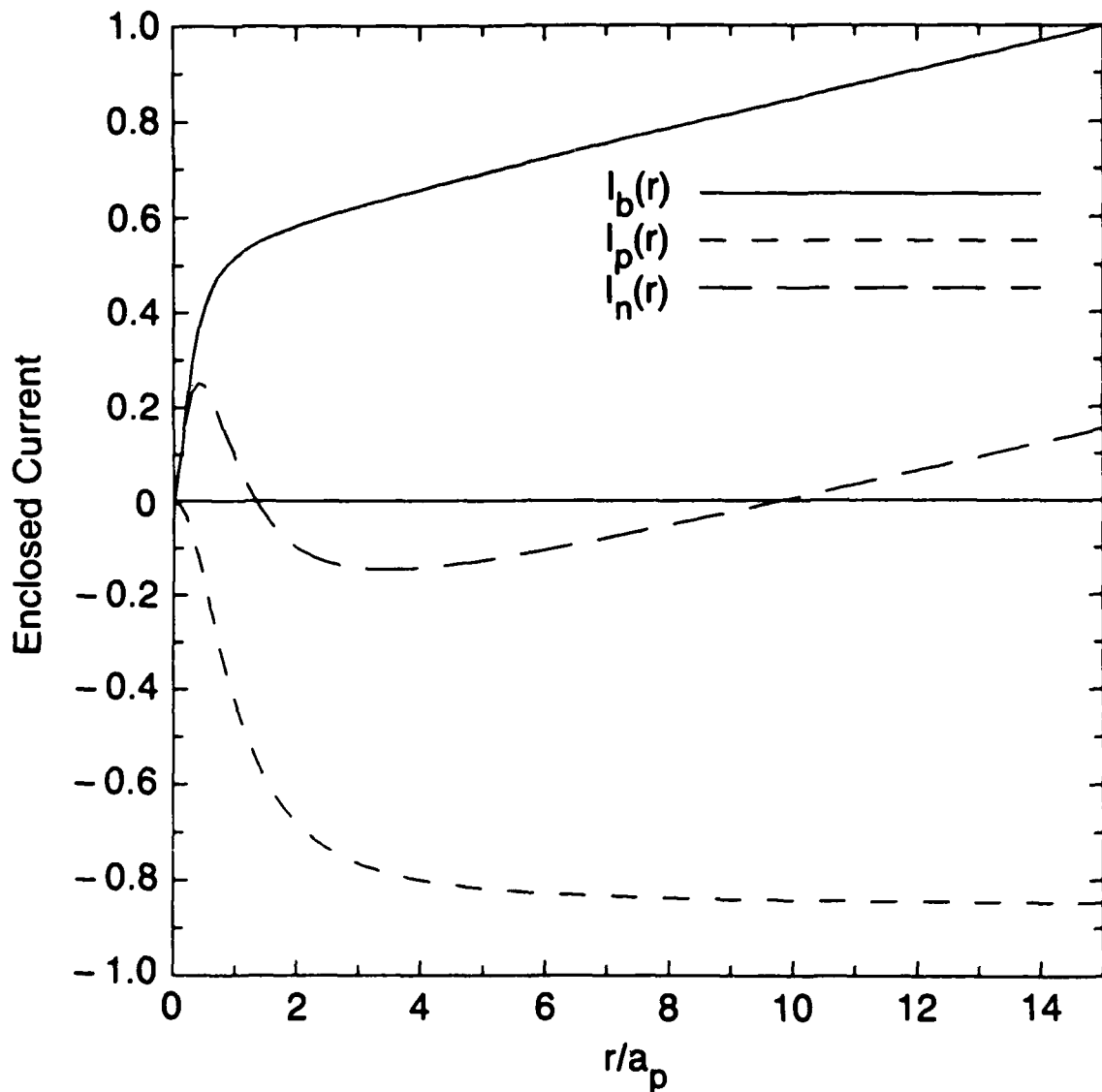


Fig. 5 Enclosed currents $I_b^{(1)}(r)$, $I_p(r)$, and $I_n^{(1)}(r)$ for a case similar to Fig. 4 but with $a_{b0}/a_p = 0.4$. Since $I_n^{(1)}(r)$ reverses sign at $r/a_p \approx 2$, this case exhibits off-axis hollowing.

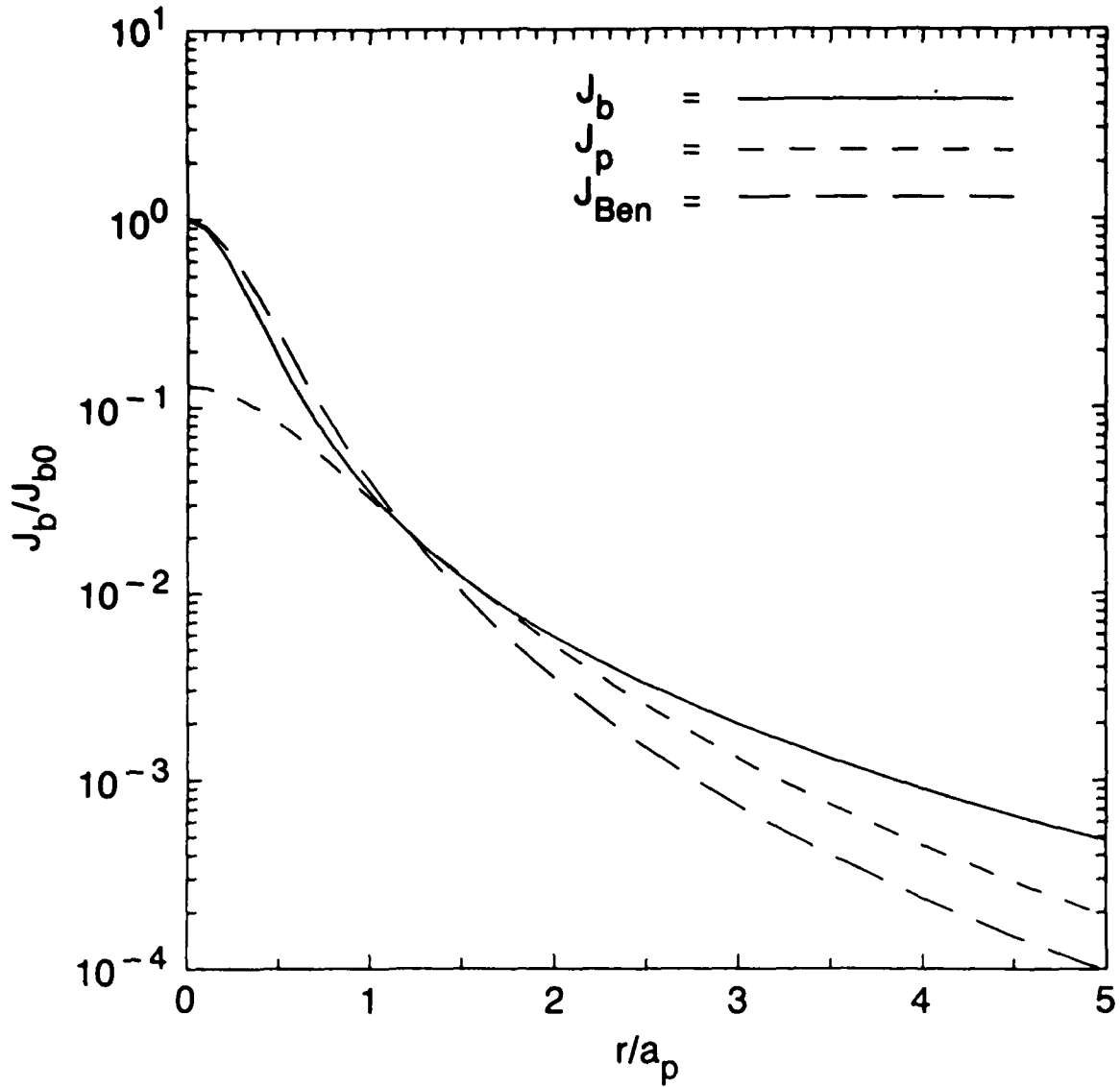


Fig. 6 Equilibrium beam current density $J_b(r)$ as obtained by direct integration of Ampere's law and the Boltzmann equilibrium condition. Also shown are $J_p(r)$, which (by fiat) has a Bennett profile with radius a_p and $J_{Ben}(r)$, a Bennett profile fitted to $J_b(r)$ in the vicinity of $r = 0$. For this case, $T/T_B = 0.6$, $1-f = 0.47$, and there is a weak halo, but overall $J_{Ben}(r)$ is a good approximation to $J_b(r)$.

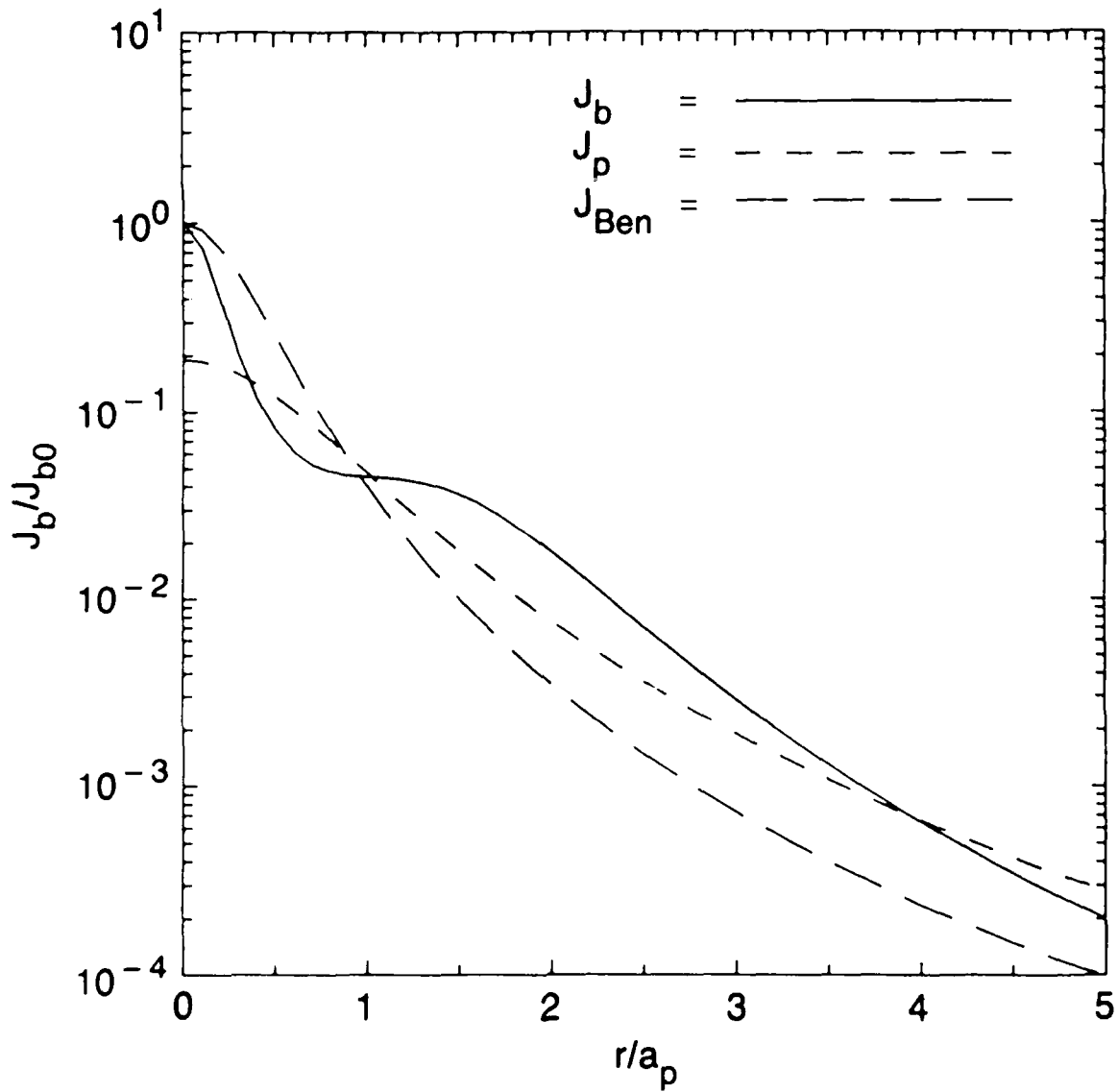


Fig. 7 Current densities $J_b(r)$, $J_p(r)$, and $J_{Ben}(r)$ for a case with $T/T_B = 0.2$ and $1 - \beta = 0.18$. $J_b(r)$ is obtained in the same manner as in Fig. 6 and exhibits a pronounced core/halo profile.

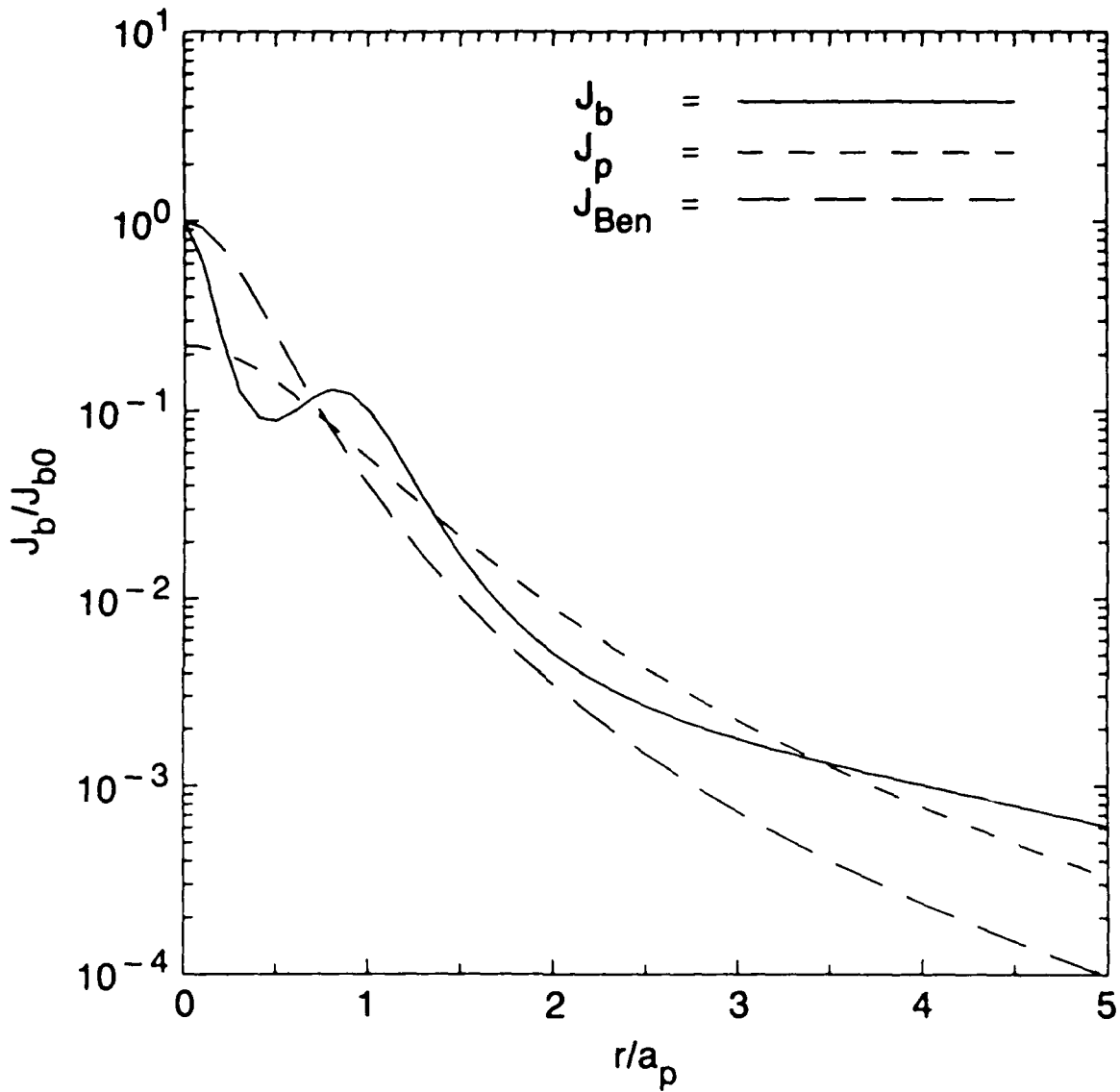


Fig. 8 Current densities $J_b(r)$, $J_p(r)$, and $J_{Ben}(r)$ for a case with $T/T_B = 0.1$ and $1-f = 0.083$. This case is similar to Fig. 7, but the larger return current results in off-axis hollowing.

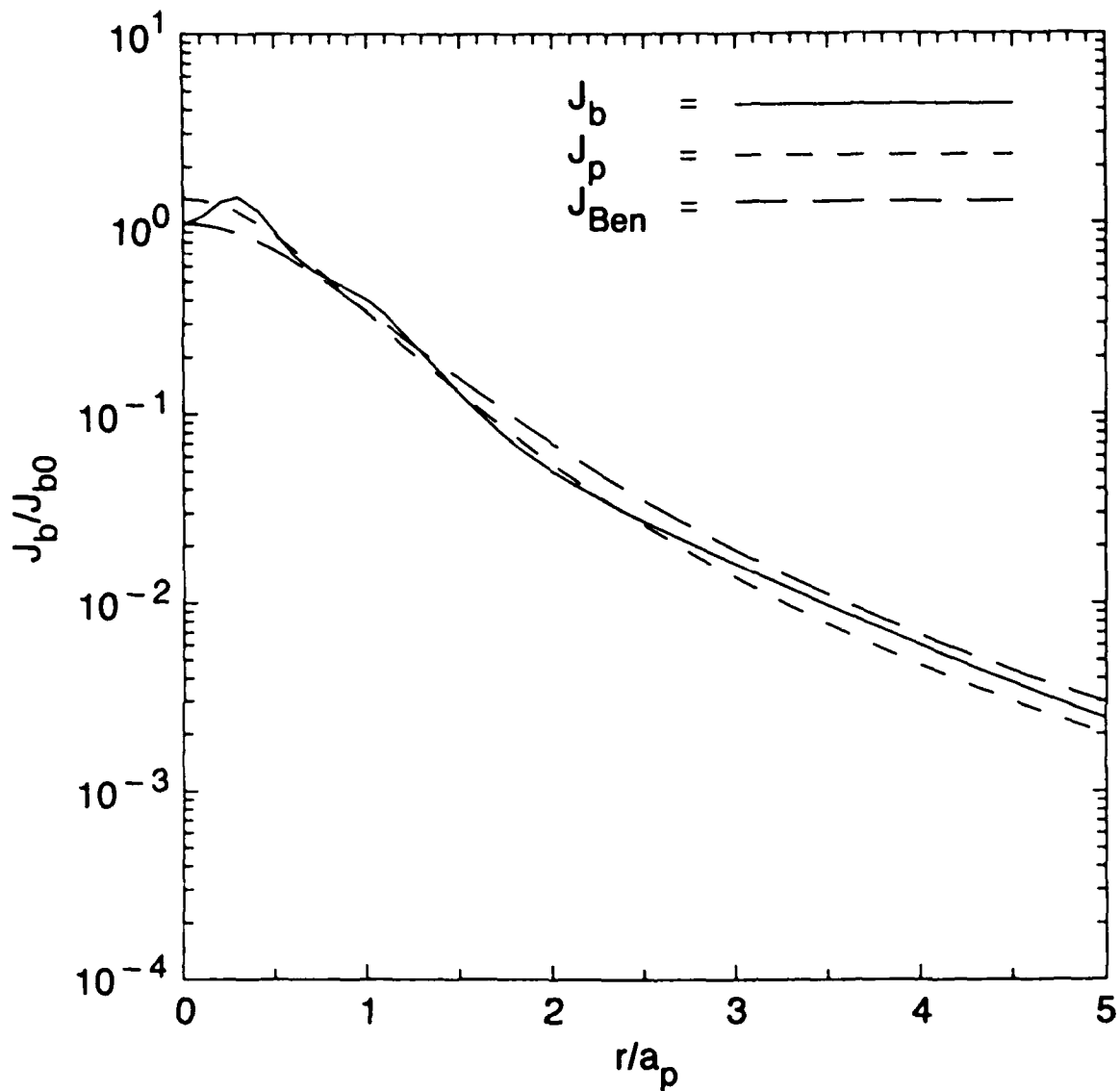


Fig. 9 Current densities $J_b(r)$, $J_p(r)$ and $J_{Ben}(r)$ for a case with $T/T_B = 0.1$ and $1-f = 0.083$. The beam current density for this case is broader than the plasma current density, and the equilibrium is hollowed on-axis. $J_b(r)$ is calculated by the same method as Fig. 6.

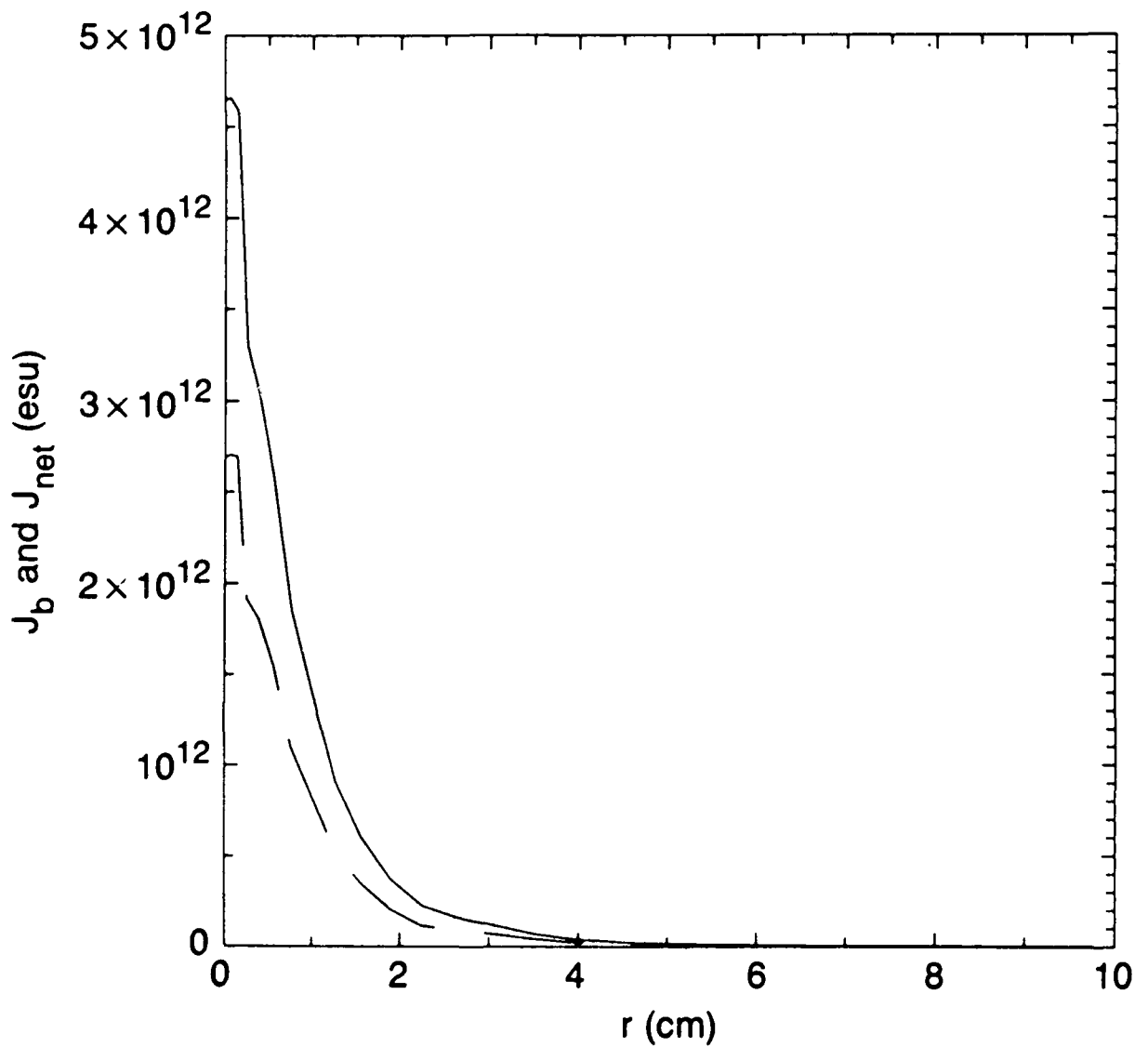


Fig. 10 Current densities $J_b(r)$ (solid line) and $J_n(r) = J_p(r) + J_b(r)$ (dashed line) taken from a SARLAC simulation of Case 1 at $\zeta = 80$ cm and $z = 240$ cm. There is no evidence for a halo or hollowing in this well-matched ($f_m = 0.5$) 10 kA case. The data is taken along the positive x-axis ($\theta = 0$), and current densities are in statamps/cm².

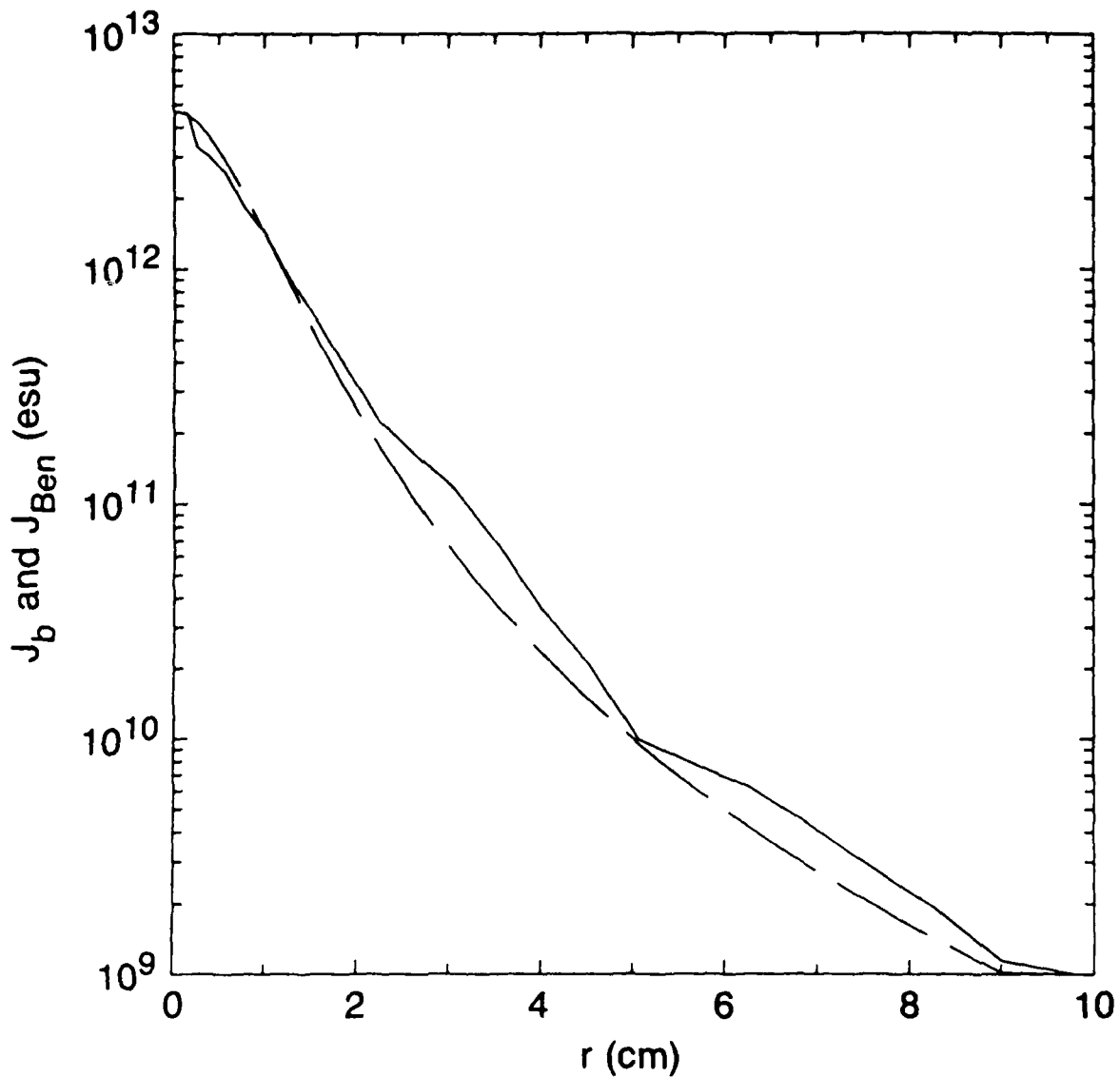


Fig. 11 Comparison of $J(r)$ (solid) and $J_{\text{Ben}}(r)$ (dashed) for the SARLAC simulation (Case 1) shown in Fig. 10. J_{Ben} is a Bennett profile fit to the current density data. The Bennett profile provides an excellent fit for this case.

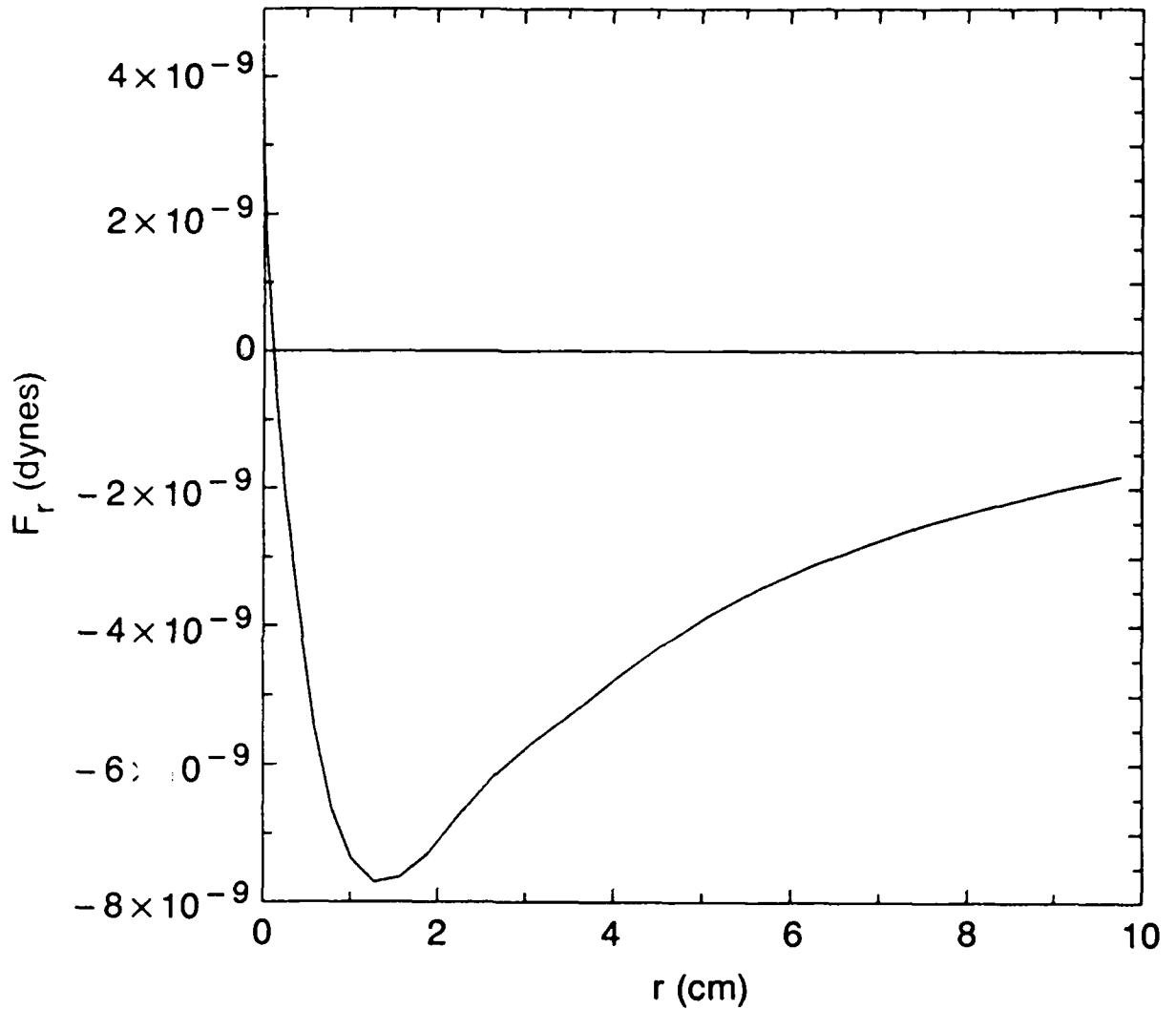


Fig. 12 Plot of the pinch force $F_r(r) = -dA(r)/dr$ for the SARLAC simulation (Case 1) shown in Fig. 10. The small region where $F_r > 0$ is due to hose-induced displacement in the +x-direction.

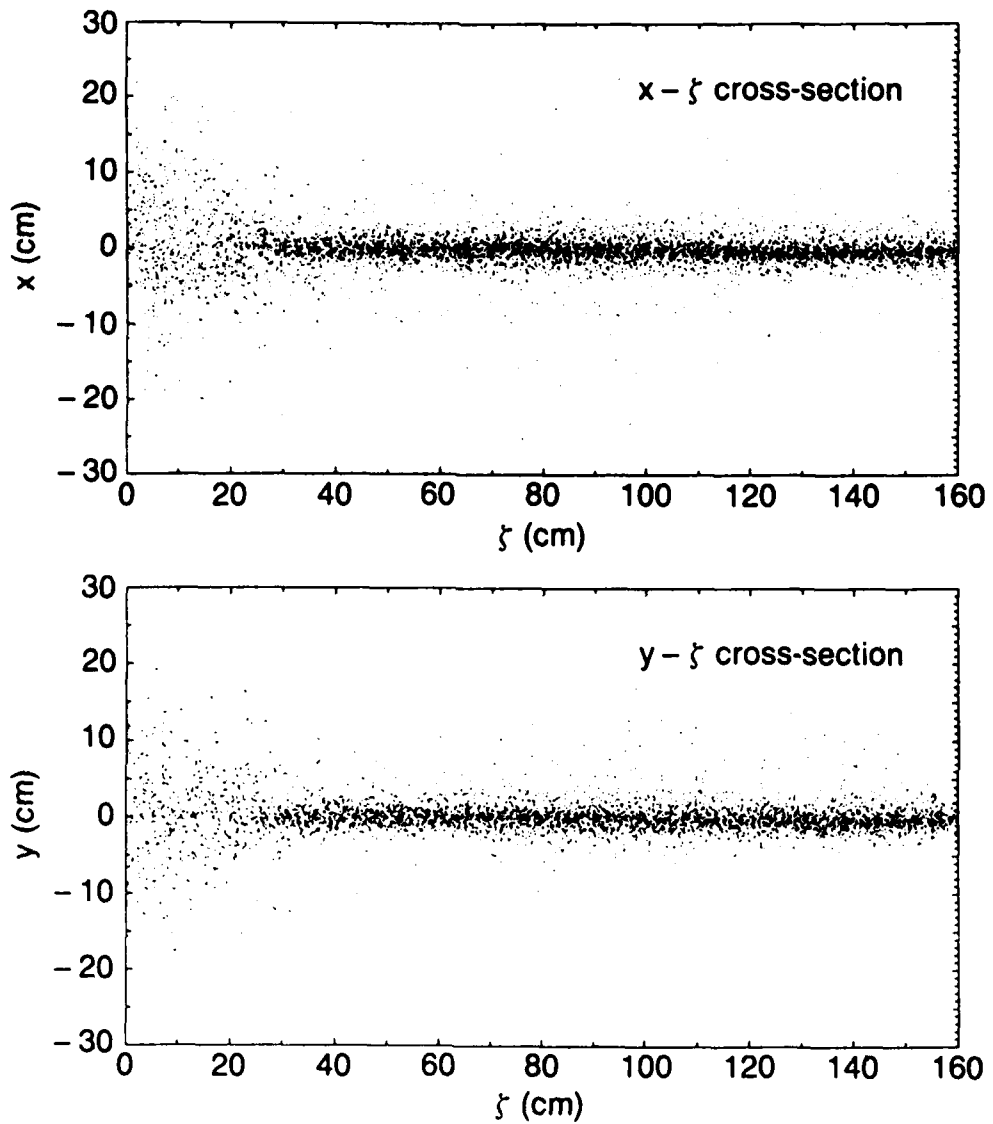


Fig. 13 Plot of the position x_i and y_i of a subset of simulation particles versus ζ for the 10 kA simulation (Case 1) shown in Figs. 10-12. At $z = 240$ cm, the beam does not show evidence for hollowing, halo formation, or large amplitude hose motion.

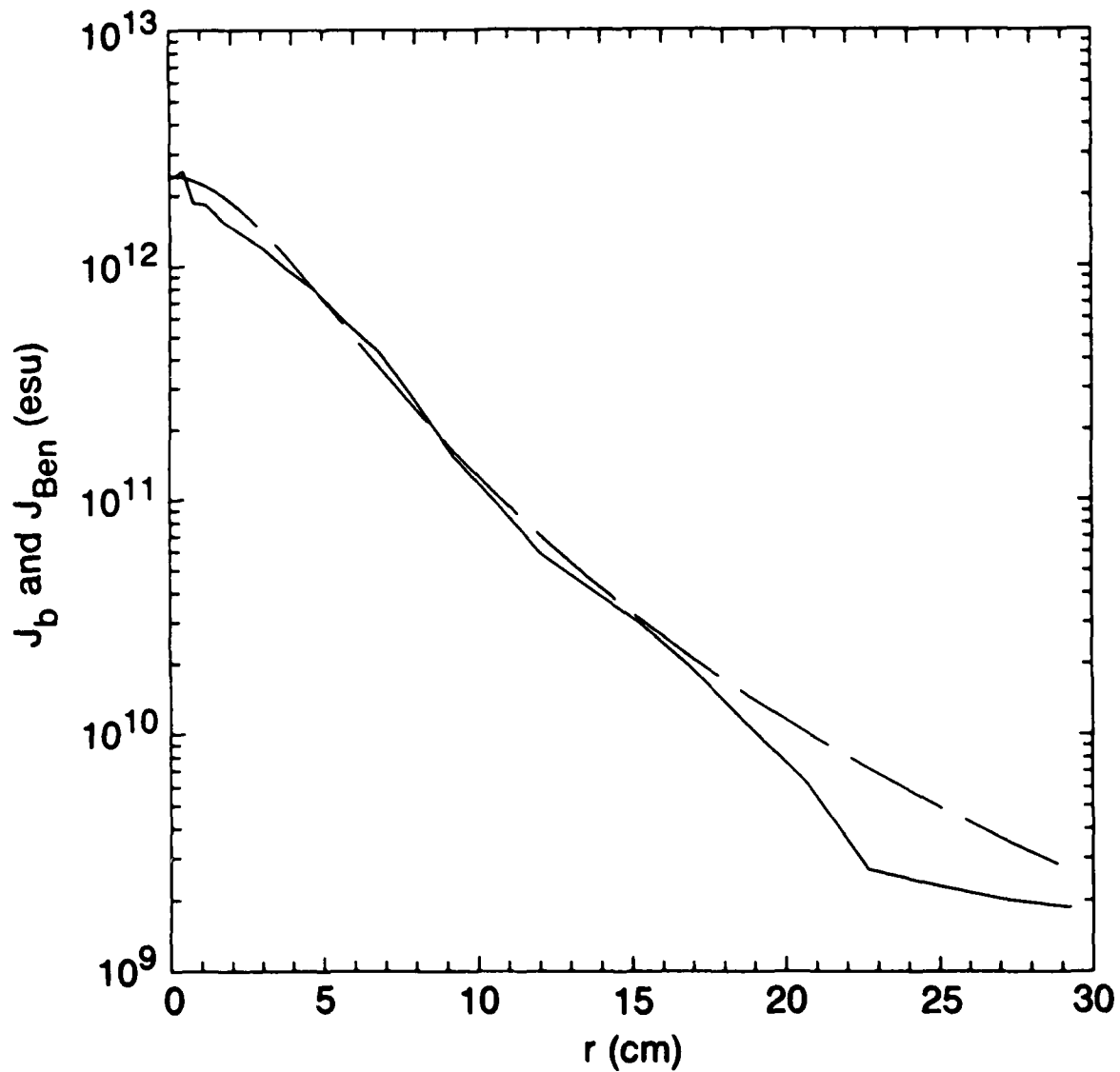


Fig. 14 Comparison of $J_b(r)$ (solid curve) and the Bennett fit $J_{Ben}(r)$ (dashed curve) from a 100 kA SARMAC simulation with a constant emittance but tapered radius at injection (Case 7). At $z = 720$ cm and $\zeta = 240$ cm, the beam profile remains Bennett-like.

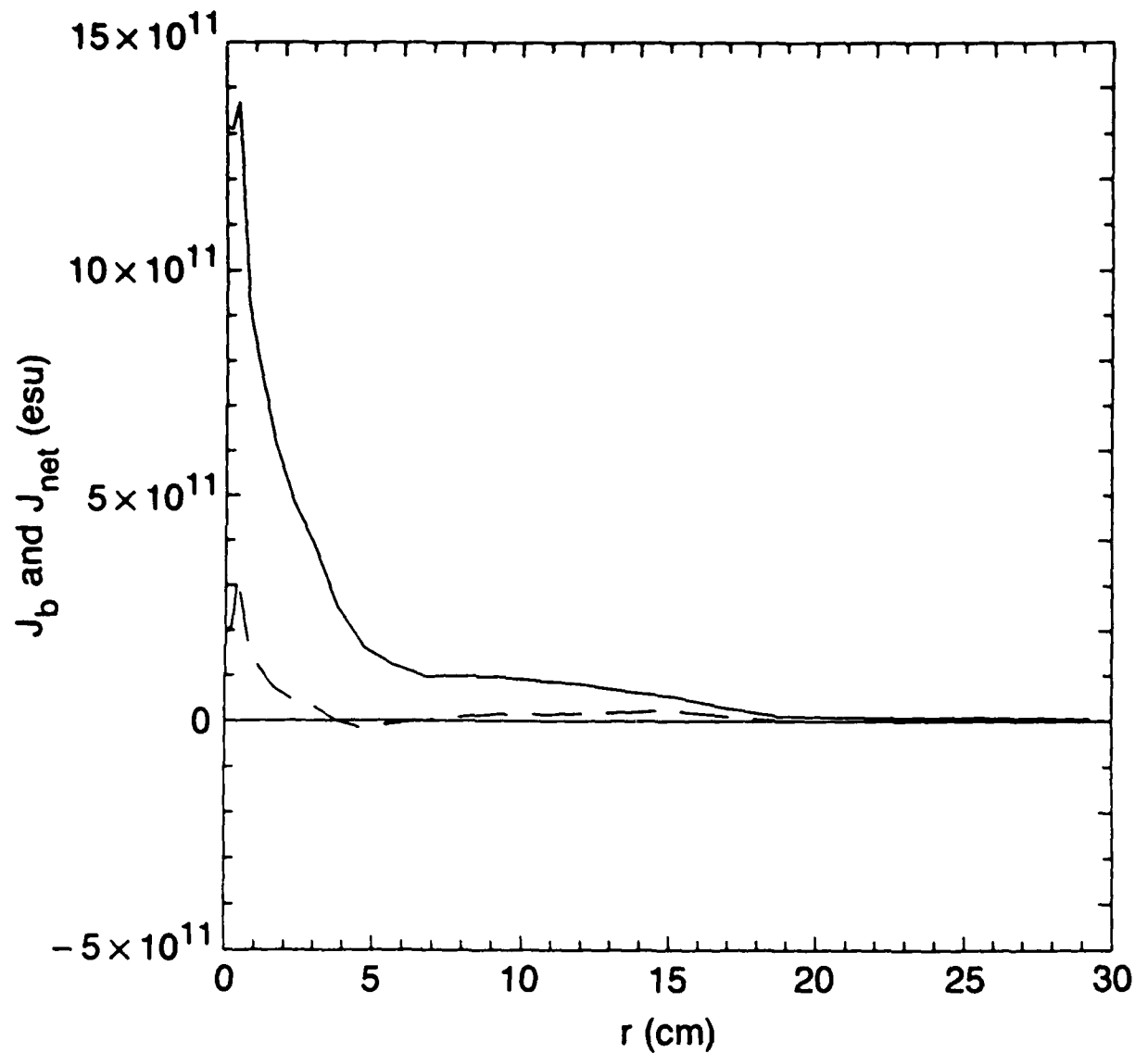


Fig. 15 Plot of $J_b(r)$ (solid curve) and $J_n(r)$ (dashed curve) from a SARLAC simulation with $I_0 = 100$ kA and $f_m = 0.4$ (Case 4). At $z = 720$ cm and $\zeta = 240$ cm, the beam forms a halo extending from 5 to 15 cm from the axis.

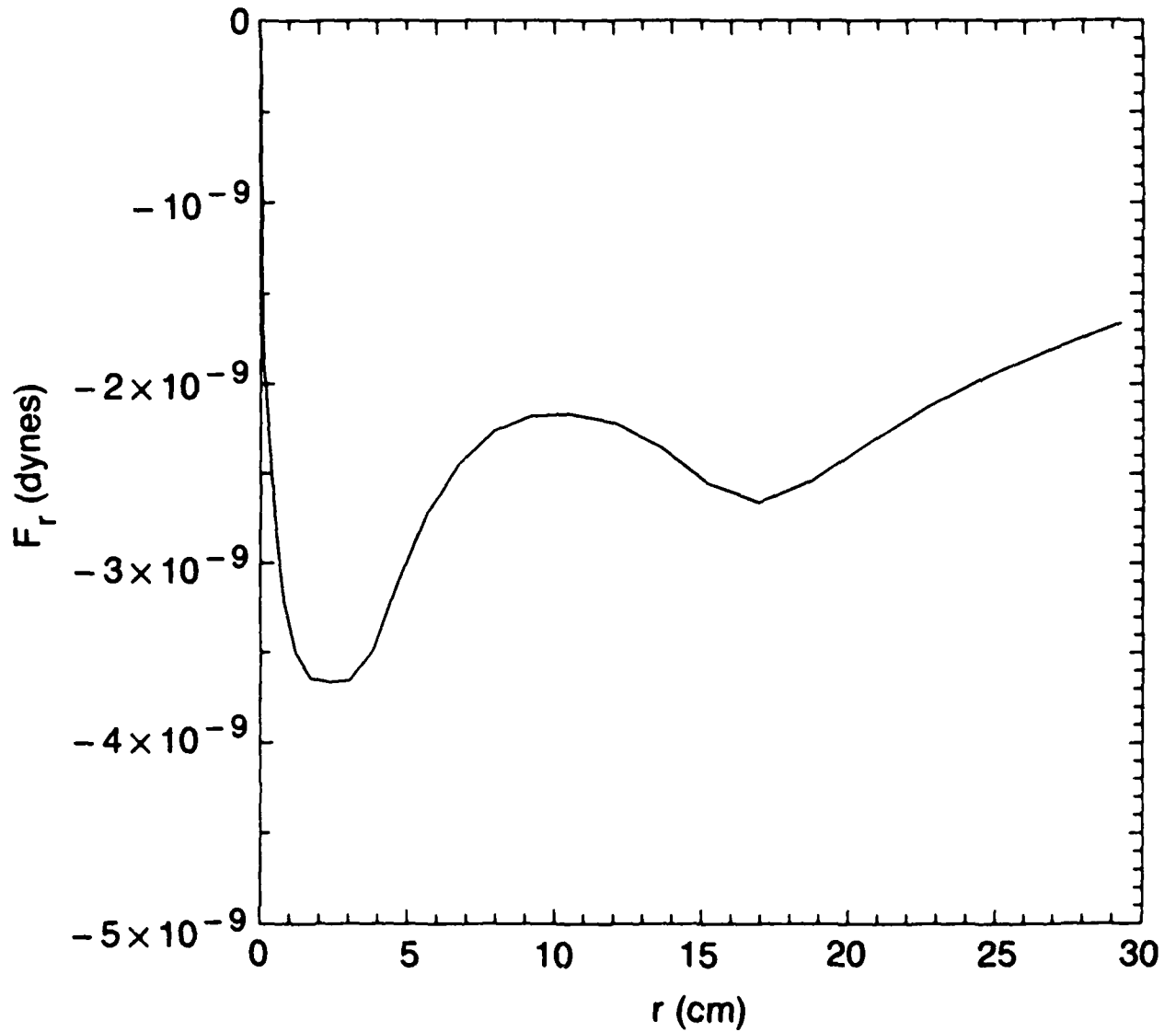


Fig. 16 Plot of pinch force $F_r(r)$ vs. r for the SARLAC simulation (Case 4) shown in Fig. 15. The halo forms in the region near the off-axis local minimum in $|F_r(r)|$.

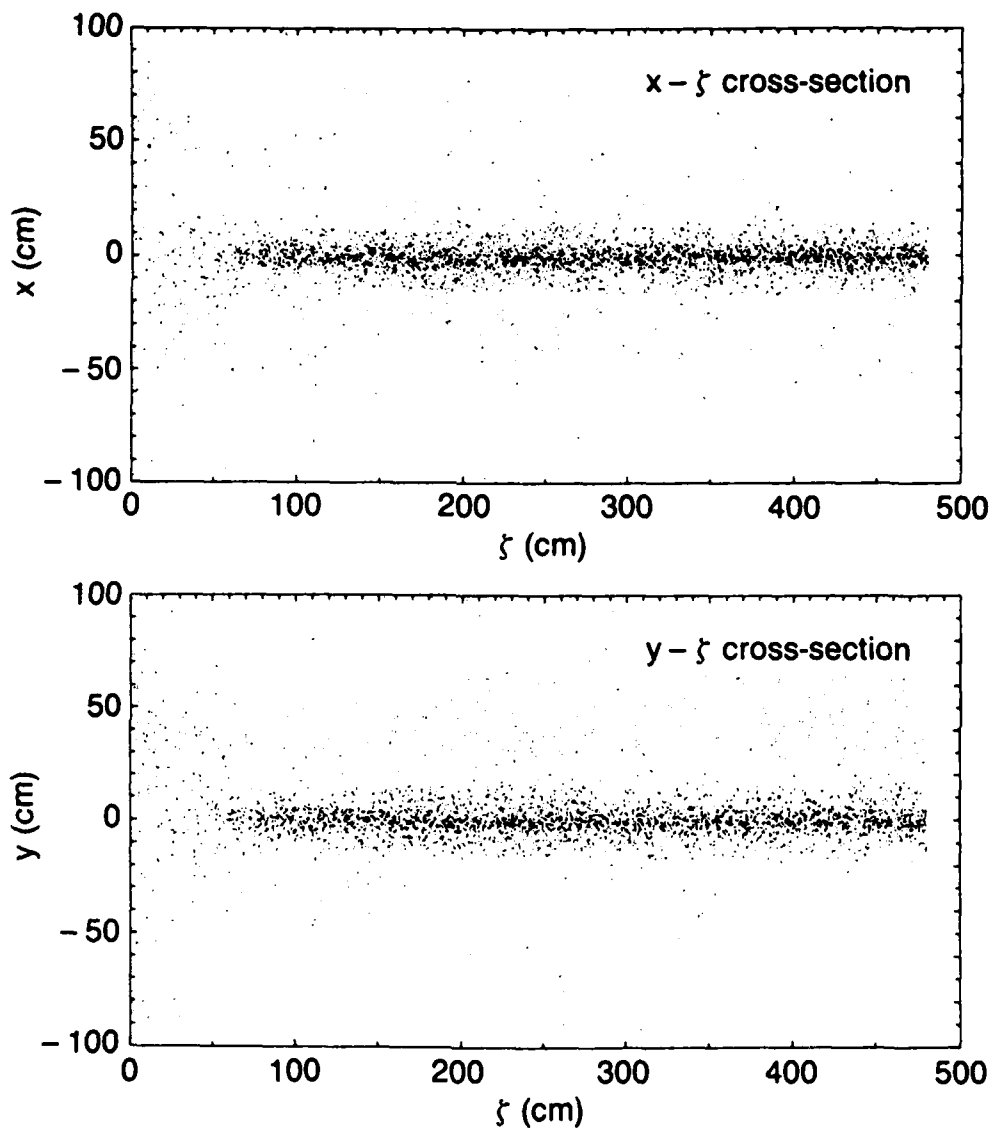


Fig. 17 Plot of simulation particle positions x_i and y_i from the core and halo example (Case 4) discussed above, taken at $z = 720$ cm. The dense core is clearly seen, and the sharp edge of the halo at 10-15 cm from the axis is also apparent.

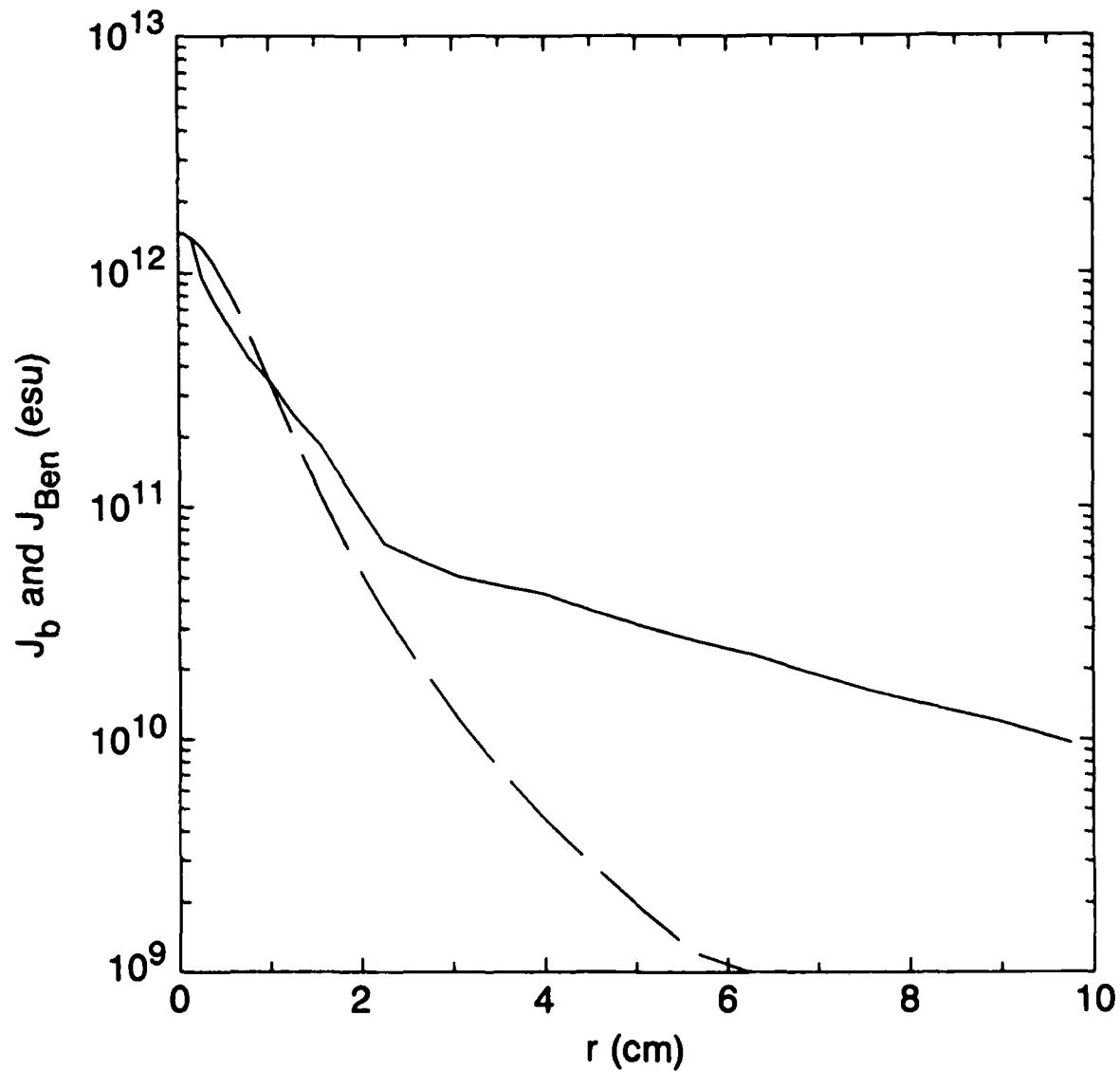


Fig. 18 An example of core and halo behavior in a poorly matched ($f_m = 1.5$) 10 kA beam. The plot of $J_b(r)$ (solid curve) and the Bennett fit $J_{Ben}(r)$ (dashed curve) are from Case 2 at $z = 240$ cm and $\zeta = 80$ cm. Most of the current flows in the halo.

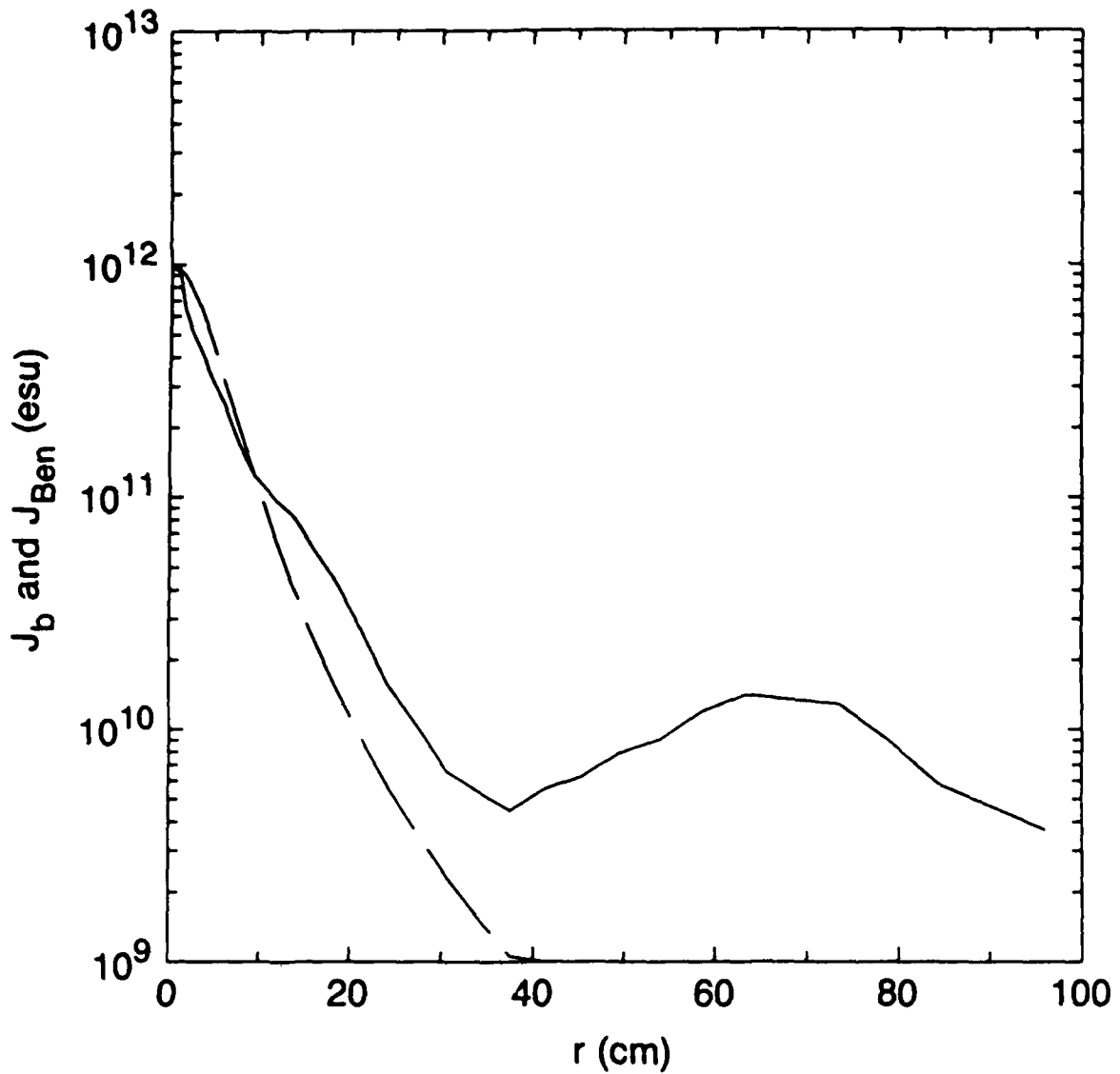


Fig. 19 An example of off-axis hollowing produced by a SARLAC simulation of a 500 kA beam (Case 8). The plots of $J_b(r)$ (solid curve) and the Bennett fit $J_{Ben}(r)$ (dashed curve) are taken along the spoke at $\theta = 7\pi/8$ which was the direction of the local maximum in $J_b(r, \theta)$. The plot is for $\zeta = 480$ cm and $z = 1200$ cm.

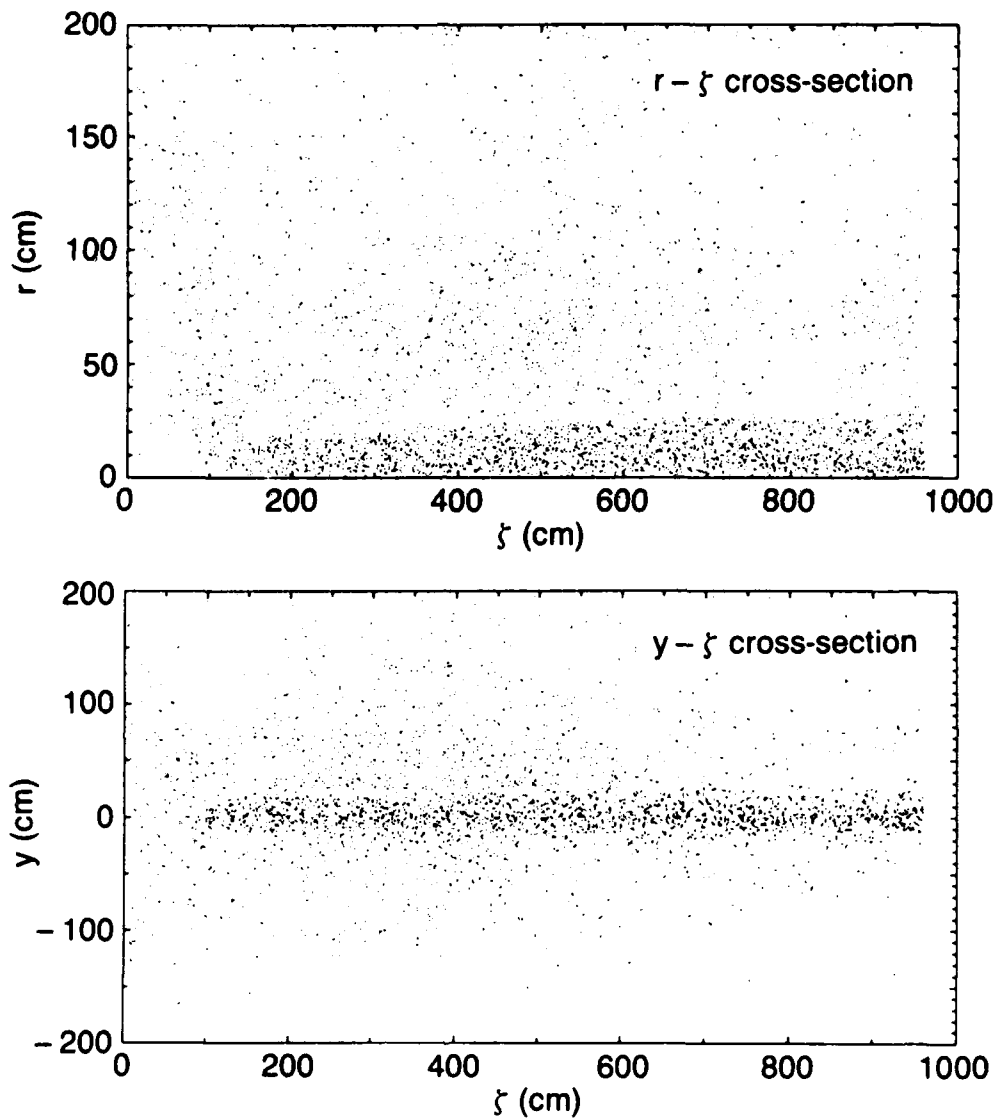


Fig. 20 Particle position plots at $z = 1200$ of the radius $r_i = (x_i^2 + y_i^2)^{1/2}$ (top of frame) and y position y_i (bottom frame) for the off-axis hollowed SARLAC simulation (Case 8) described in Fig. 19.

A gap in particles is apparent in the r_i plot at the top edge of the denser band at 20-25 cm from the axis. Geometrical factors obscure the gap when viewed from the side (bottom frame).

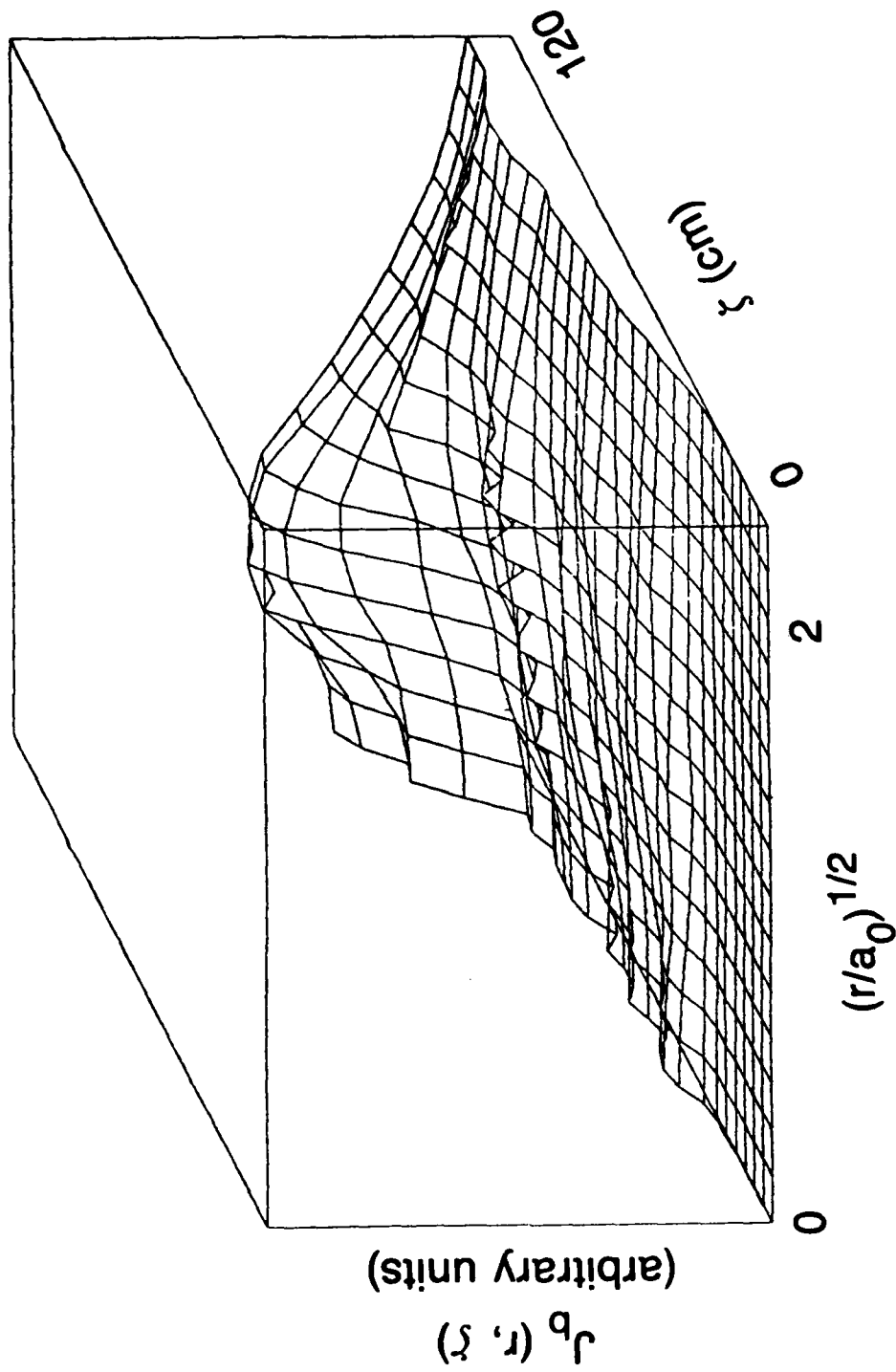


Fig. 21 An example of on-axis hollowing observed in a SIMMØ simulation of a 10 kA beam propagating in a reduced-density channel. The plot of $J_b((r/a_0)^{1/2}, z/a_0)$ in arbitrary units is taken at $z = 800 a_0$, and $a_0 = 0.5$ cm.

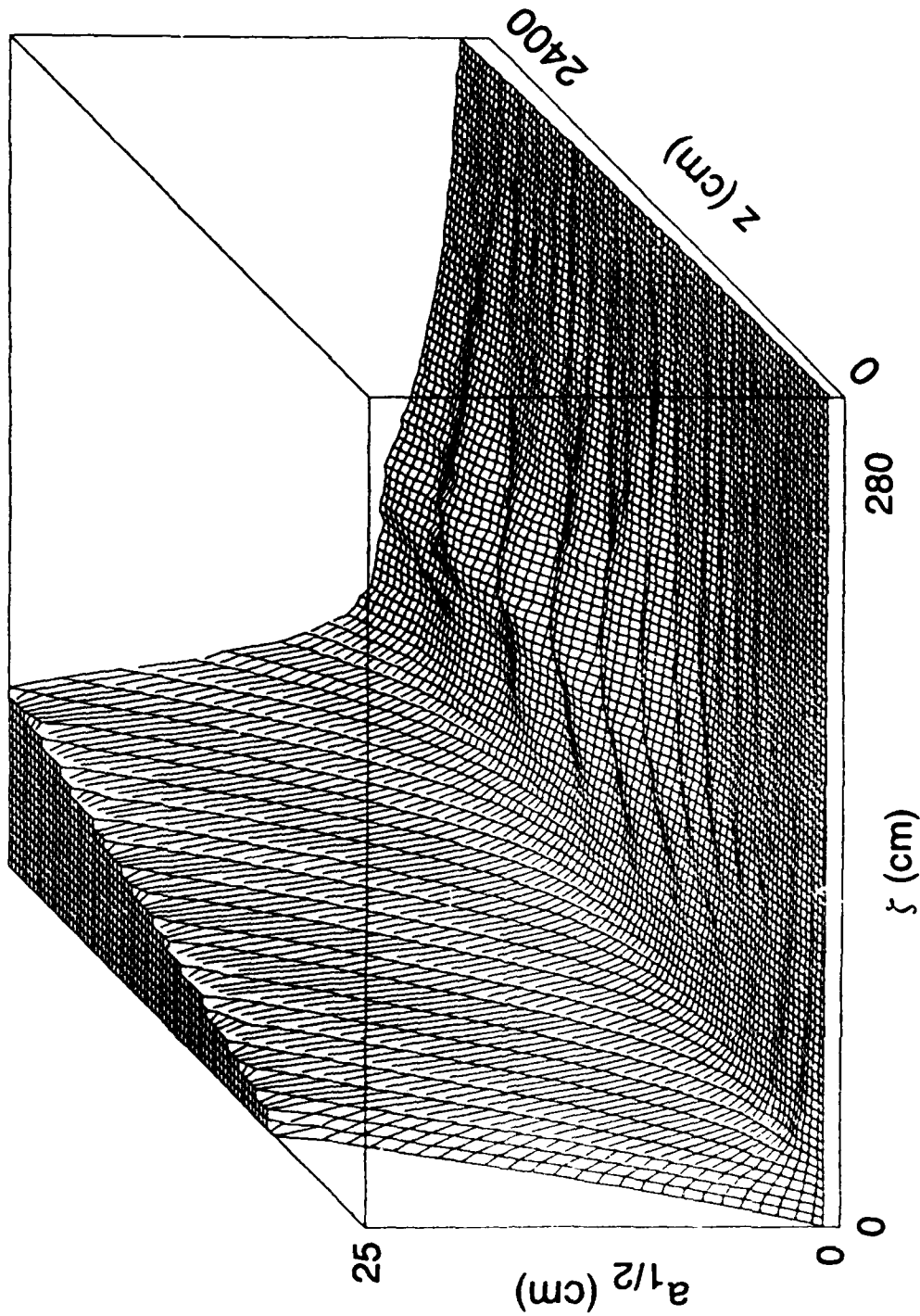


Fig. 22 A surface plot of the beam radius $a(\zeta, z)$ for the on-axis hollowed example described in Fig. 21. Although the radius shows some oscillations, there is no evidence for the violent disruption which is often associated with the axisymmetric hollowing instability.

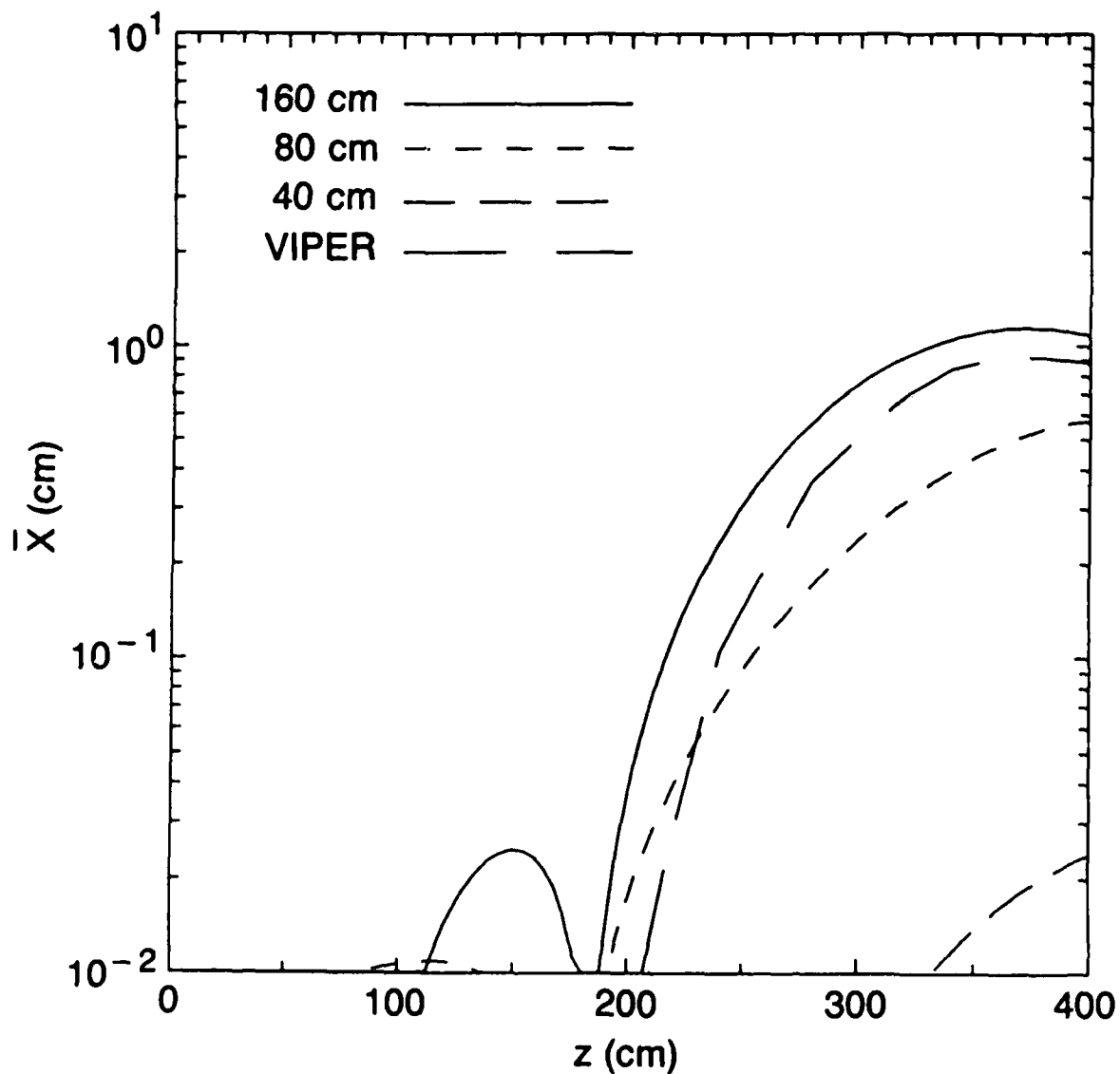


Fig. 23 Beam displacement $\bar{X}(z)$ taken from simulations of a well-matched 10 kA beam (Case 1). The three SARLAC curves are for $\zeta = 40, 80,$ and 160 cm, and the VIPER curve is $\zeta = 160$ cm. As expected for this Bennett-like example, the SARLAC hose instability displacement at $\zeta = 160$ cm agrees well with the VIPER result.

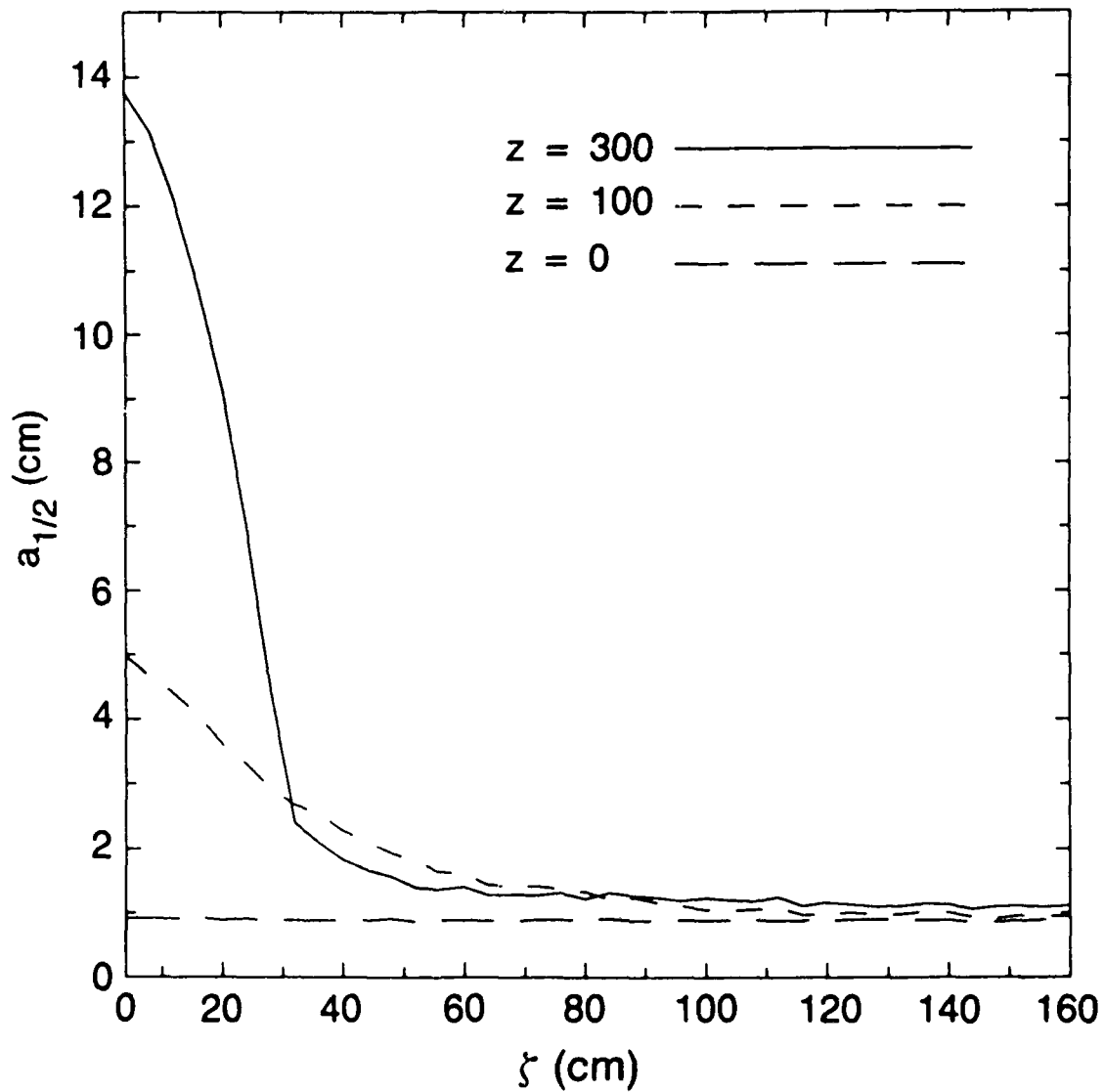


Fig. 24 Beam radius $a_{1/2}(\zeta)$ for $z = 0, 100, \text{ and } 300$ cm for the SARLAC simulation (Case 1) shown in Fig. 23. Except in the expanded beam head, the beam radius remains almost constant.

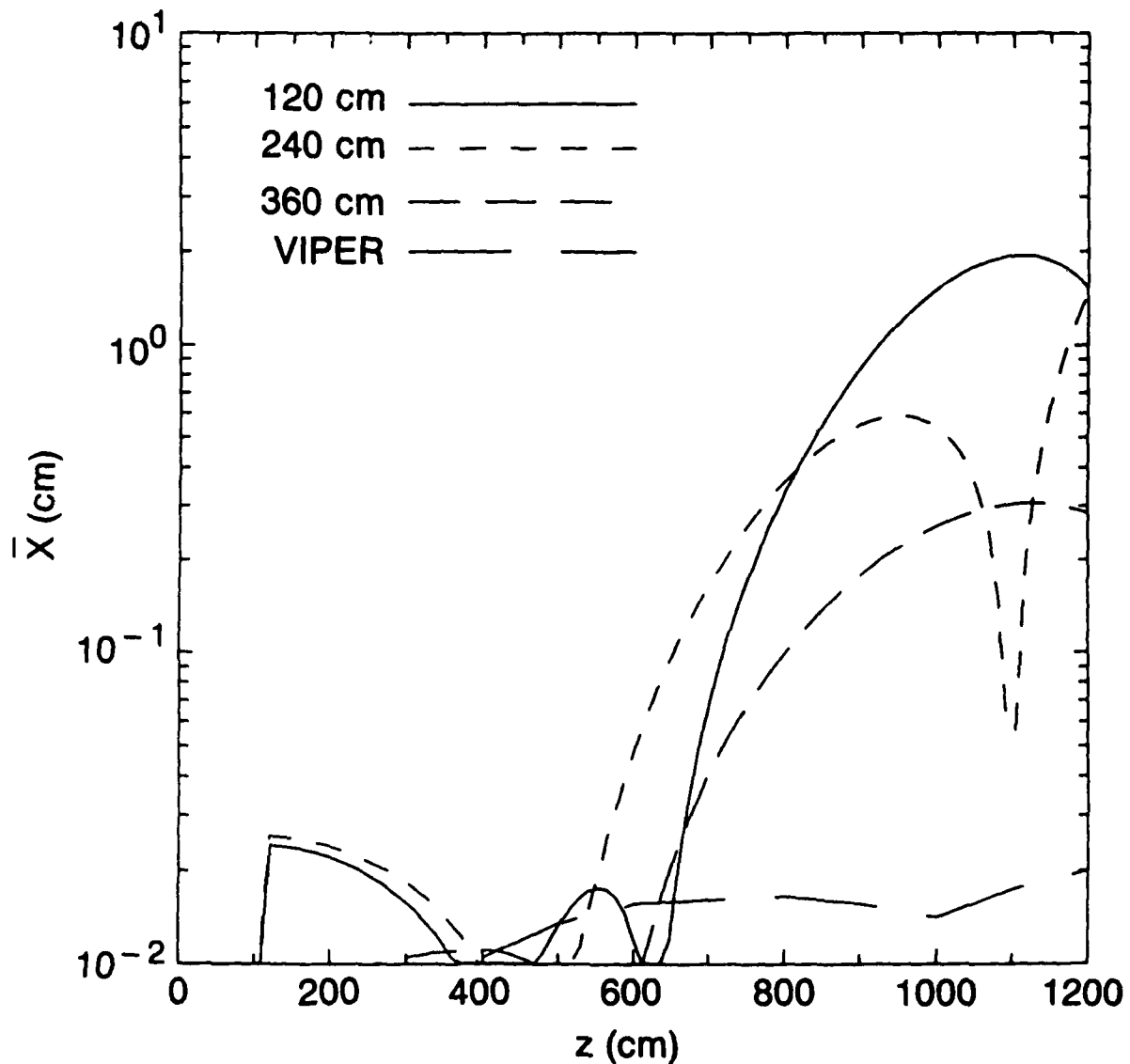


Fig. 25 Beam displacement $\bar{X}(z)$ at $\zeta = 120, 240,$ and 360 cm taken from a SARLAC simulation of a 100 kA beam (Case 4) which exhibits core and halo behavior. Also shown is the result from a VIPER simulation at $\zeta = 360$ cm. In this comparison, the SARLAC model predicts much more hose growth than does VIPER.

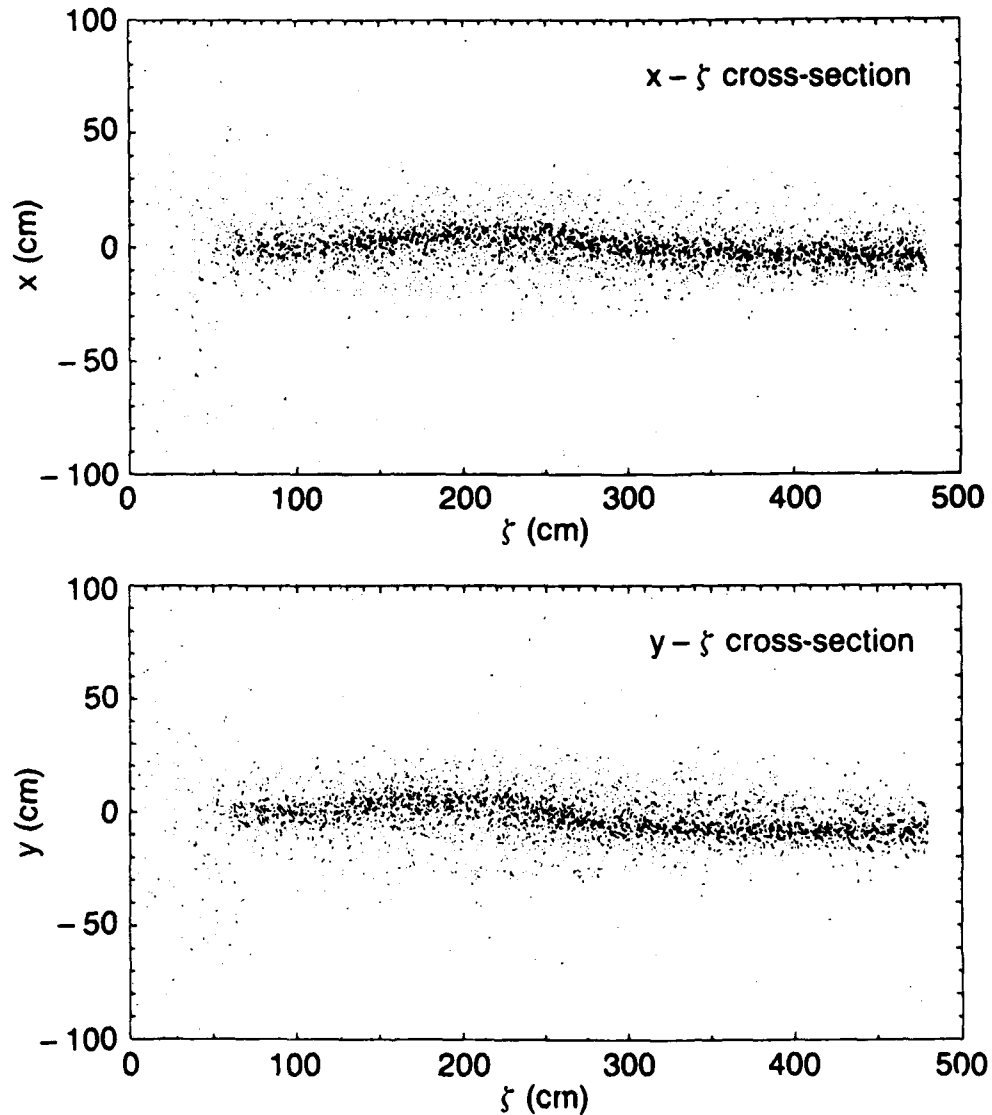


Fig. 26 Simulation particle positions for the core and halo example (Case 4) taken at $z = 1200$ cm. The hose instability distortions of the beam core are clearly observable. (In Fig. 17, which was taken from the same simulation at a shorter propagation distance, the instability had not yet grown into the large amplitude regime).

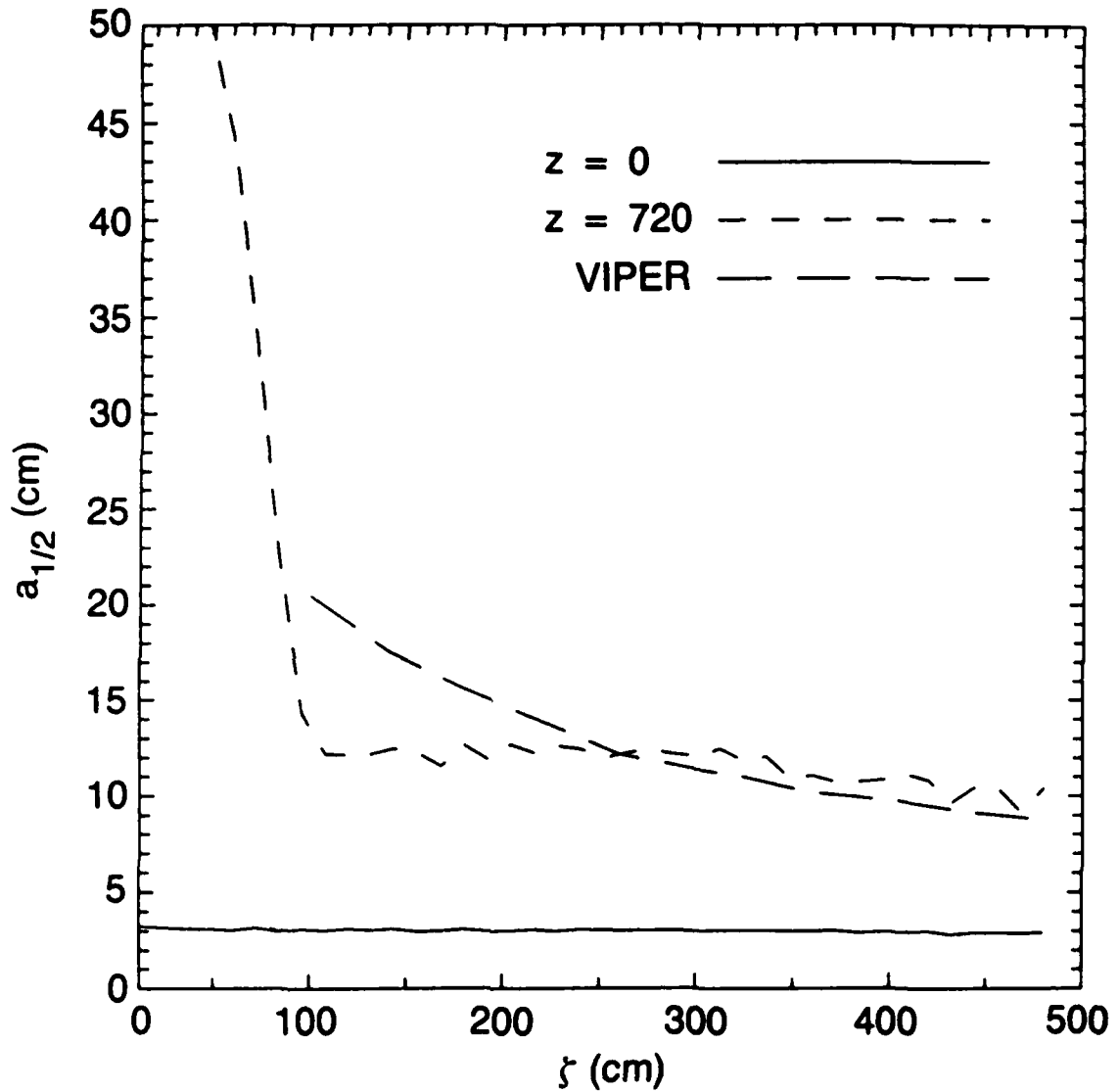


Fig. 27 Beam radius $a_{1/2}(z)$ for the core and halo simulation (Case 4) shown in Figs. 25 and 26. At $z = 720$ cm, the half current radius from the SARLAC code quickly reaches a nearly constant value of 10-12 cm, although the core radius is much smaller ($\sim a_0 = 3$ cm). The VIPER code at $z = 720$ cm predicts a beam radius which tapers significantly.

Distribution List*

Naval Research Laboratory
4555 Overlook Avenue, S.W.

Attn: CAPT W. G. Clautice - Code 1000
Dr. M. Lampe - Code 4792 (20 copies)
Dr. T. Coffey - Code 1001
Head, Office of Management & Admin - Code 1005
Director of Technical Services - Code 2000
NRL Historian - Code 2604
Dr. J. Boris - Code 4040
Dr. M. Picone - Code 4040
Dr. M. Rosen - Code 4650
Dr. M. Haftel - Code 4665
Dr. S. Ossakov - Code 4700 (26 copies)
Dr. A. Ali - Code 4700.1
Dr. M. Friedman - Code 4700.1
Dr. R. Taylor - BRA (4700.1)
Mr. I. M. Vitkovitsky - Code 4701
Dr. S. Gold - Code 4740
Dr. R. Meger - Code 4750
Dr. A. Robson - Code 4760
Dr. D. Murphy - Code 4763
Dr. R. Pechacek - Code 4763
Dr. D. Taggart - Code 4763
Dr. G. Cooperstein - Code 4770
Dr. D. Colombant - Code 4790
Dr. R. Fernsler - Code 4790
Dr. I. Haber - Code 4790
Dr. R. F. Hubbard - Code 4790
Dr. G. Joyce - Code 4790
Dr. Y. Lau - Code 4790
Dr. S. P. Slinker - Code 4790
Dr. P. Sprangle - Code 4790
W. Brizzi - Code 4790A
Code 4790 (20 copies)
Library - Code 2628 (20 copies)
D. Wilbanks - Code 2634
Code 1220

* Every name listed on distribution gets one copy except for those where extra copies are noted.

Air Force Office of Scientific Research
Physical and Geophysical Sciences
Bolling Air Force Base
Washington, DC 20332
Attn: Major Bruce Smith

Air Force Weapons Laboratory
Kirtland Air Force Base
Albuquerque, NM 87117
Attn: V. Baker (AFWL/NTYP)
D. Dietz (AFWL/NTYP)
Lt Col J. Head

U. S. Army Ballistics Research Laboratory
Aberdeen Proving Ground, Maryland 21005
Attn: Dr. Donald Eccleshall (DRXBR-BM)
Dr. Anand Prakash

Avco Everett Research Laboratory
2385 Revere Beach Pkwy
Everett, Massachusetts 02149
Attn: Dr. R. Patrick
Dr. Dennis Reilly

Ballistic Missile Def. Ad. Tech. Ctr.
P.O. Box 1500
Huntsville, Alabama 35807
Attn: Dr. M. Hawie (BMSATC-1)

Chief of Naval Material
Office of Naval Technology
MAT-0712, Room 503
800 North Quincy Street
Arlington, VA 22217
Attn: Dr. Eli Zimet

Cornell University
369 Upson Hall
Ithaca, NY 14853
Attn: Prof. David Hammer

DASIAC - DETIR
Kaman Tempo
25600 Huntington Avenue, Suite 500
Alexandria, VA 22303
Attn: Mr. F. Wimenitz

Defense Advanced Research Projects Agency
1400 Wilson Blvd.
Arlington, VA 22209
Attn: Dr. Shen Shey
Dr. H. L. Buchanan

Department of Energy
Washington, DC 20545
Attn: Dr. Wilmot Hess (ER20:GTN,
High Energy and Nuclear Physics)
Mr. Gerald J. Peters (G-256)

Directed Technologies, Inc.
8500 Leesburg Pike, Suite 601
Vienna, VA 22180
Attn: Dr. Ira P. Kuhn
Dr. Nancy Chesser

C. S. Draper Laboratories
555 Technology Square
Cambridge, Massachusetts 02139
Attn: Dr. E. Olsson
Dr. L. Matson

General Dynamics Corporation
Pomana Division
1675 W. Mission Blvd.
P. O. Box 2507
Pomana, CA 92769-2507
Attn: Dr. Ken W. Hawko

Hy-Tech Research Corp.
P. O. Box 3422 FSS
Radford, VA 24143
Attn: Dr. Edward Yadlowsky

HQ Foreign Technology Division
Wright-Patterson AFB, OH 45433
Attn: TUTD/Dr. C. Joseph Butler

Institute for Fusion Studies
University of Texas at Austin
RLM 11.218
Austin, TX 78712
Attn: Prof. Marshall N. Rosenbluth

Intelcom Rad Tech.
P.O. Box 81087
San Diego, California 92138
Attn: Dr. W. Selph

Joint Institute for Laboratory
Astrophysics
National Bureau of Standards and
University of Colorado
Boulder, CO 80309
Attn: Dr. Arthur V. Phelps

Kaman Sciences
1500 Garden of the Gods Road
Colorado Springs, CO 80933
Attn: Dr. John P. Jackson

La Jolla Institute
P. O. Box 1434
La Jolla, CA 92038
Attn: Dr. K. Brueckner

Lawrence Berkeley Laboratory
University of California
Berkeley, CA 94720
Attn: Dr. Edward P. Lee

Lawrence Livermore National Laboratory
University of California
Livermore, California 94550
Attn: Dr. Richard J. Briggs
Dr. Simon S. Yu
Dr. Frank Chambers
Dr. James W.-K. Mark, L-477
Dr. William Fawley
Dr. William Barletta
Dr. William Sharp
Dr. Daniel S. Prono
Dr. John K. Boyd
Dr. Kenneth W. Struve
Dr. John Clark
Dr. George J. Caporaso
Dr. William E. Martin
Dr. Donald Prosnitz

Lockheed Missiles and Space Co.
3251 Hanover St.
Bldg. 205, Dept 92-20
Palo Alto, CA 94304
Attn: Dr. John Siambis

Los Alamos National Scientific Laboratory
P.O. Box 1663
Los Alamos, NM 87545
Attn: Dr. L. Thode
Dr. H. Dogliani, MS-5000
Dr. R. Carlson
Ms. Leah Baker, MS-P940
Dr. Carl Ekdahl
Dr. Joseph Mack

Maxwell Laboratories Inc.
8888 Balboa Avenue
San Diego, CA 92123
Attn: Dr. Ken Whitham

McDonnell Douglas Research Laboratories
Dept. 223, Bldg. 33, Level 45
Box 516
St. Louis, MO 63166
Attn: Dr. Evan Rose
Dr. Carl Leader
Dr. Frank Bieniosek

Mission Research Corporation
1720 Randolph Road, S.E.
Albuquerque, NM 87106
Attn: Dr. Brendan Godfrey
Dr. Thomas Hughes
Dr. Lawrence Wright
Dr. Barry Newberger
Dr. Michael Mostrom
Dr. Dale Welch

Mission Research Corporation
P. O. Drawer 719
Santa Barbara, California 93102
Attn: Dr. C. Longmire
Dr. N. Carron

National Bureau of Standards
Gaithersburg, Maryland 20760
Attn: Dr. Mark Wilson

Naval Surface Warfare Center
White Oak Laboratory
Silver Spring, Maryland 20903-5000
Attn: Dr. R. Cavley
Dr. J. W. Forbes
Dr. B. Hui
Mr. W. M. Hinckley
Mr. N. E. Scofield
Dr. E. C. Whitman
Dr. M. H. Cha
Dr. H. S. Uhm
Dr. R. Fiorito
Dr. K. T. Nguyen
Dr. R. Stark
Dr. R. Chen
Dr. D. Rule

Office of Naval Research
800 North Quincy Street
Arlington, VA 22217
Attn: Dr. C. W. Roberson
Dr. F. Saalfeld

Office of Naval Research (2 copies)
Department of the Navy
Code 01231C
Arlington, VA 22217

Office of Under Secretary of Defense
Research and Engineering
Room 3E1034
The Pentagon
Washington, DC 20301
Attn: Dr. John MacCallum

ORI, Inc.
1375 Piccard Drive
Rockville, MD 20850
Attn: Dr. C. M. Huddleston

Physics International, Inc.
2700 Merced Street
San Leandro, CA. 94577
Attn: Dr. E. Goldman

Princeton University
Plasma Physics Laboratory
Princeton, NJ 08540
Attn: Dr. Francis Perkins, Jr.

Pulse Sciences, Inc.
600 McCormack Street
San Leandro, CA 94577
Attn: Dr. Sidney Putnam
Dr. John Bayless

The Rand Corporation
2100 M Street, NW
Washington, DC 20037
Attn: Dr. Nikita Wells
Mr. Simon Kassel

Sandia National Laboratory
Albuquerque, NM 87115
Attn: Dr. David Hasti/1272
Dr. Collins Clark
Dr. John Freeman/1241
Dr. Charles Frost
Dr. George Kamin/1274
Dr. Gordon T. Leifeste
Dr. Gerald N. Hays
Dr. James Chang
Dr. Michael G. Mazerakis/1272
Dr. John Wagner/1241
Dr. Ron Lipinski/1274

Science Applications Intl. Corp.
P. O. Box 2351
La Jolla, CA 92038
Attn: Dr. Rang Tsang

Science Applications Intl. Corp.
5150 El Camino Road
Los Altos, CA 94022
Attn: Dr. R. R. Johnston
Dr. Leon Feinstein
Dr. Douglas Keeley

Science Applications Intl. Corp.
1710 Goodridge Drive
McLean, VA 22102
Attn: Mr. V. Chadsey
Dr. A Drobot
Dr. K. Papadopoulos

Commander
Space & Naval Warfare Systems Command
PMW-145
Washington, DC 20363-5100
Attn: CAPT J. D. Fontana
LT Fritchie

SRI International
PSO-15
Molecular Physics Laboratory
333 Ravenswood Avenue
Menlo Park, CA 94025
Attn: Dr. Donald Eckstrom
Dr. Kenneth R. Stalder

Strategic Defense Initiative Org.
1717 H Street, N. W.
Washington, DC 20009
Attn: Lt Col R. L. Gullickson
Dr. J. Ionson
Dr. D. Duston

Strategic Defense Initiative Office
Directed Energy Weapons Office, The
Pentagon
Office of the Secretary of Defense
Washington, DC 20301-7100
Attn: Dr. C. F. Sharn (OP0987B)

Titan Systems, Inc.
9191 Towne Centre Dr.-Suite 500
San Diego, CA 92122
Attn: Dr. R. M. Dove

University of California
Physics Department
Irvine, CA 92664
Attn: Dr. Gregory Benford

University of Maryland
Physics Department
College Park, MD 20742
Attn: Dr. Y. C. Lee
Dr. C. Grebogi

University of Michigan
Dept. of Nuclear Engineering
Ann Arbor, MI 48109
Attn: Prof. Terry Kamash
Prof. R. Gilgenbach

Director of Research
U.S. Naval Academy
Annapolis, MD 21402 (2 copies)

Records 1 copy